Asynchronous formation of the adjacent epithermal Au-Cu and porphyry Cu-Mo deposits in the Zijinshan orefield, southeast China

Article *in* Ore Geology Reviews · September 2018

DOI: 10.1016/j.oregeorev.2018.09.023

CITATIONS
0

READS
180

6 authors, including:

Wenting Huang
Guangzhou institute of geochemistry
27 PUBLICATIONS **122** CITATIONS
SEE PROFILE

Huaying Liang
Chinese Academy of Sciences
82 PUBLICATIONS **1,726** CITATIONS
SEE PROFILE

Lei Wu
Curtin University
8 PUBLICATIONS **17** CITATIONS
SEE PROFILE

Zhiwei Bao
Chinese Academy of Sciences
83 PUBLICATIONS **2,365** CITATIONS
SEE PROFILE

Ore Geology Reviews 102 (2018) 351–367

Contents lists available at ScienceDirect

Ore Geology Reviews

journal homepage: www.elsevier.com/locate/oregeorev

Asynchronous formation of the adjacent epithermal Au-Cu and porphyry Cu-Mo deposits in the Zijinshan orefield, southeast China

Wenting Huang[a], Huaying Liang[a,*], Lei Wu[b], Jing Wu[c], Jing Li[d], Zhiwei Bao[a]

[a] Key Laboratory of Mineralogy and Metallogeny, Guangzhou Institute of Geochemistry, Chinese Academy of Sciences, 511 Kehua Street, Wushan, Guangzhou 510640, China
[b] Earth Dynamics Research Group, The Institute for Geoscience Research (TIGeR), Department of Applied Geology, Curtin University, Perth 6845, Australia
[c] College of Resource and Metallurgy, Guangxi University, Nanning, Guangxi 530004, China
[d] Zijin Mining Group Co, Ltd, Shanghang 364200, China

ARTICLE INFO

Keywords:
High sulfidation epithermal deposit
Porphyry copper deposit
Zijinshan
Southern China

ABSTRACT

Adjacent high-sulfidation epithermal (HSE) and porphyry deposits often have similar Cu-Au metal association, suggesting they are cogenetic and formed contemporaneously. The Zijinshan orefield (ZOF) is the largest Au producer in China and contains a series of HSE Au-Cu and porphyry Cu-Mo deposits. This study presents new (1) muscovite ^{40}Ar-^{39}Ar ages for the HSE deposit in this area, new (2) zircon laser ablation-inductively coupled plasma-mass spectrometry (LA-ICP-MS) U-Pb ages for felsic igneous rocks associated with the epithermal and porphyry mineralization, and (3) new zircon Lu-Hf isotopic data for these intrusions, all of which provides insights into why these adjacent epithermal Au-Cu and porphyry Cu-Mo deposits have different metal associations.

The age data indicate that the alunite-dickite alteration related to the HSE Au-Cu mineralization formed before ca. 110 Ma and the main HSE Au-Cu mineralizing event occurred at ca. 113 Ma. In comparison, the adjacent porphyry Cu-Mo mineralization formed at ca. 104 Ma, ca. 9 Myr after the HSE event. The volcanic rocks associated with the HSE Au-Cu mineralization yield zircon ε_{Hf} (t) values from −4.1 to 0.3, whereas the Cu-Mo mineralized porphyry has lower zircon ε_{Hf} (t) values (−4.5 to −1.2), suggesting that the magmas that formed the latter intrusion were derived from a source containing more crustal material than the magmas associated with the HSE mineralization. The differences in the timing of mineralization and the sources of the magmas indicate that the adjacent HSE and porphyry deposits in the ZOF formed from different magmatic-hydrothermal systems that controlled the different metal associations of the mineralizing systems. This means that future mineral exploration within the ZOF should target porphyry Au-Cu deposit at depths that is genetically related to the HSE Au-Cu deposit. The results also show that not all adjacent porphyry and epithermal deposits, especially those with different metal associations, are cogenetic.

1. Introduction

Porphyry and high-sulfidation epithermal (HSE) mineralizing systems represent important sources of Cu, Mo, and Au (Heinrich et al., 1999; Ulrich et al., 1999; Halter et al., 2002) and are commonly closely spatially associated (e.g., Arribas et al., 1995; Sillitoe, 1997, 2010; Hedenquist et al., 1998; Chang et al., 2011; Cooke et al., 2011). A genetic link has been proposed for these types of mineral deposits (e.g., Sillitoe, 1989; Hedenquist and Lowenstern, 1994; Gammons and WilliamsJones, 1997; Muntean and Einaudi, 2001; Heinrich, 2003; Heinrich et al., 2004; John et al., 2010; Hedenquist and Taran, 2013; Bissig and Cooke, 2014). Cogenetic porphyry and HSE deposits usually have similar Cu and Au metal associations (e.g., Muntean and Einaudi, 2001; Pudack et al., 2009; Teal and Benavides, 2010; Deyell and Hedenquist, 2011; Franchini et al., 2011; Waters et al., 2011; Maydagan et al., 2015, Table 1) because both Cu and Au can be transported as stable chloride complexes in high-temperature saline fluids (Hemley and Hunt, 1992) before they coprecipitate (Ulrich et al., 1999; Heinrich et al., 2004). Such cogenetic deposits form contemporaneously, as evidenced by ages that are within uncertainty of each other (e.g., Arribas et al., 1995; Muntean and Einaudi, 2001; Table 1).

The Zijinshan orefield (ZOF) is located in Fujian Province and is the richest Au-Cu mining area in southeast China (Zhang, 2013; Fig. 1). Several epithermal and porphyry deposits have been identified within

* Corresponding author.
E-mail address: lianghy@gig.ac.cn (H. Liang).

https://doi.org/10.1016/j.oregeorev.2018.09.023
Received 26 March 2018; Received in revised form 24 August 2018; Accepted 20 September 2018
Available online 21 September 2018
0169-1368/

Table 1
Global examples of co-genetic porphyry and high-sulfidation epithermal deposits.

Country	District	Deposit	Metals association	Age/mineral(s)-method(s)	References
Philippines	Baguio	Ampucao-Hartwell-Balatoc cluster porphyry prospects	Cu-Au	0.51 ± 0.26 to 1.09 ± 0.10 Ma/Hornblende $^{40}Ar/^{39}Ar$	Waters et al. (2011)
		Acupan epithermal deposit	Au (Cu)	0.65 ± 0.07 Ma/Illite K-Ar	Cooke et al. (2011)
	Mankayan	Far Southeast porphyry	Cu-Au	1.22 ± 0.06 to 1.45 ± 0.04 Ma/Biotite and Illite K-Ar	Arribas et al. (1995)
		Lapanto HSE	Cu-Au	1.17 ± 0.16 to 1.56 ± 0.29 Ma/Alunite K-Ar	Deyell and Hedenquist (2011)
Argentina	Altar	Porphyry	Cu (Au-Mo)	10.35 ± 0.32 to 11.75 ± 0.24 Ma/Zircon U-Pb	Maydagan et al. (2015)
		HSE	Cu-Au-Ag	–	
	Famatina	Nevados de Famatina porphyry	Cu-Mo-Au	–	Pudack et al. (2009)
		La Mejicana HSE	Cu-Au-(Ag)	–	
	Agua Rica	Porphyry	Cu (Mo-Au)	5.10 ± 0.05 Ma/Biotite K–Ar	Franchini et al. (2011)
		HSE	Cu-Au	4.88 ± 0.08 Ma/Alunite K-Ar	Perelló et al. (1998)
Peru	Yanacocha	Porphyry	Au-Cu	10.7 Ma/Biotite $^{40}Ar/^{39}Ar$	Teal and Benavides (2010)
		HSE	Au (Cu)	8.5 to 11.5 Ma/Alunite $^{40}Ar/^{39}Ar$	Longo et al. (2010)
Chile	Refugio	Verde Porphyry	Au (Cu)	23.3 Ma/Biotite $^{40}Ar/^{39}Ar$	Muntean and Einaudi (2001)
		Pancho HSE	Au (Ag)	23.2 Ma/Biotite $^{40}Ar/^{39}Ar$	
	Aldebaran	Cerro Casale Porphyry	Au (Cu)	13.89 Ma/Biotite $^{40}Ar/^{39}Ar$	
		Vein zone HSE	Au (Ag)	13.91 Ma/Alunite $^{40}Ar/^{39}Ar$	
	La Pepa	Cavancha Porphyry	Au (Cu)	23.8 Ma/Biotite $^{40}Ar/^{39}Ar$	
		Purpura and Liebre HSE	Au (Ag)	23.5 Ma/Alunite $^{40}Ar/^{39}Ar$	
Iran	Sari Gunay	Porphyry mineralization	Cu-Au	10.3–10.8 Ma/Sericite $^{40}Ar/^{39}Ar$	Richards et al. (2006)
		Epithermal	Au	11.0–11.7 Ma/Biotite and Hornblende $^{40}Ar/^{39}Ar$	
Russia	Birgilda-Tomino	Kalinovskoe porphyry	Cu-(Au)	429.8 ± 4.8 Ma/Molybdenite Re-Os	Tessalina and Plotinskaya (2017);
		Bereznyakovskoe HSE	Ag-Au-(Cu)	427 ± 6 Ma/Zircon U-Pb	Grabezhev et al. (2013)

the ZOF, including the Zijinshan HSE Au-Cu deposit, which is the largest epithermal deposit in China, and the Luoboling porphyry Cu-Mo deposit, which represents the largest porphyry deposit in southeast China (Zhang, 2013). These two HSE and porphyry deposits are thought to be cogenetic, forming from the same magmatic-hydrothermal system (So et al., 1998; Zhang et al., 2001; 2002; Wang et al., 2009, 2013; Jiang et al., 2013; Zhong et al., 2014; Li et al., 2017; Jiang et al., 2017; Piquer et al., 2017). However, this cogenetic model for the ZOF is unlikely to be correct for a number of reasons. Firstly, the Zijinshan HSE deposit has a Au-Cu metal association, whereas the adjacent Luoboling porphyry deposit has a Cu-Mo metal association but contains low concentrations of Au (< 0.1 ppm). This pair of HSE Au-Cu and porphyry Cu-Mo deposits is different from the majority of adjacent and cogenetic HSE and porphyry deposits that have similar Au-Cu associations (Heinrich et al., 2004). Secondly, the cogenetic model is not supported by age data, as the porphyry mineralization is thought to have formed at ca. 104 Ma (e.g., Liang et al., 2012; Zhong et al., 2014), whereas the timing of epithermal mineralization remains poorly constrained. Published ages for the Zijinshan HSE deposit range from 124 to 82 Ma and were obtained from K-Ar dating of low-temperature alteration minerals and the Rb-Sr dating of fluid inclusions, respectively (Zhang et al., 1991, 2005; Chen, 1996; Zhou and Chen, 1996; Mao et al., 2002). Consequently, a more accurate and precise age for the timing of formation of the epithermal mineralization is key to understand whether the Zijinshan Au-Cu HSE deposit and the Luoboling Cu-Mo porphyry are cogenetic.

This study presents new robust muscovite ^{40}Ar-^{39}Ar ages for the Zjinshan HSE deposit and a new zircon U-Pb age for the Luoboling porphyry deposit, and uses these data to investigate the relationship between the deposits. We also determined the zircon Hf isotopic composition of a series of igneous rocks in the ZOF to understand variation in the sources of magmas associated with the deposits and their contrasting metal associations.

2. Geological setting

The ZOF is located in the eastern part of the Cathaysian fold belt in southeast China (Fig. 1B). This region contains numerous epithermal and porphyry deposits, including the giant Zijinshan HSE Au-Cu deposit, the large Longjiangting intermediate-sulfidation epithermal Cu-Ag-Au deposit, the large Yueyang low-sulfidation Ag-Au-Cu deposit, the small Wuziqilong Cu-Ag (Au) deposit, the large Luoboling porphyry Cu-Mo deposit, the small Jinmei porphyry Cu-Mo deposit and the Ermiaogou epithermal Cu (Au) deposit (Fig. 1C). These deposits contain a total of 399 tons of Au, 6.400 thousand tons of Ag, 4.137 million tons of Cu, and 110 thousand tons of Mo (Zhang, 2013).

The oldest units within the ZOF are the fault-bounded metamorphosed clastic units of the Neoproterozoic Louziba Group that crop out in the northwestern and southeastern parts of the area (Fig. 1C). These rocks are unconformably overlain by Late Devonian and Carboniferous sediments. The Early Cretaceous Shimaoshan Group volcanics also crop out across the ZOF (Fig. 1C), although the majority of these volcanics within the central ZOF have been eroded away during post-volcanic uplift. The volcanics are sparsely distributed and are dominated by welded breccias, crypto-explosive breccias, tuffs (Zhang et al., 2001; Xiao et al., 2012), and porphyritic dacite (Hu et al., 2012). The central ZOF contains a dacitic volcanic dome that is closely associated with the Zijinshan HSE Au-Cu deposit. The volcanic rocks of the Shimaoshan Group within the ZOF yield zircon LA-ICP-MS U-Pb and Rb-Sr isochrone ages of 113–93 Ma (Hu et al., 2012; Xiao et al., 2012; Jiang et al., 2013) and 125–73 Ma (Zhang et al., 2001), respectively.

The Mesozoic intrusions in the ZOF are dominated by the Zijinshan granite complex, the Caixi monzogranite, the Sifang granodiorite and the Luoboling granodiorite porphyry. The Zijinshan granitic complex crops out in the central ZOF and records three phases of magmatism (Fig. 1) with zircon U-Pb ages of 154–165 Ma (Zhang et al., 2001; Mao et al., 2004; Zhao et al., 2008; Xiao et al., 2012; Jiang et al., 2013; Yu et al., 2013; Wu et al., 2016). The Caixi monzogranite corps out in the eastern ZOF and yields zircon U-Pb ages of 157–150 Ma (Zhao et al.,

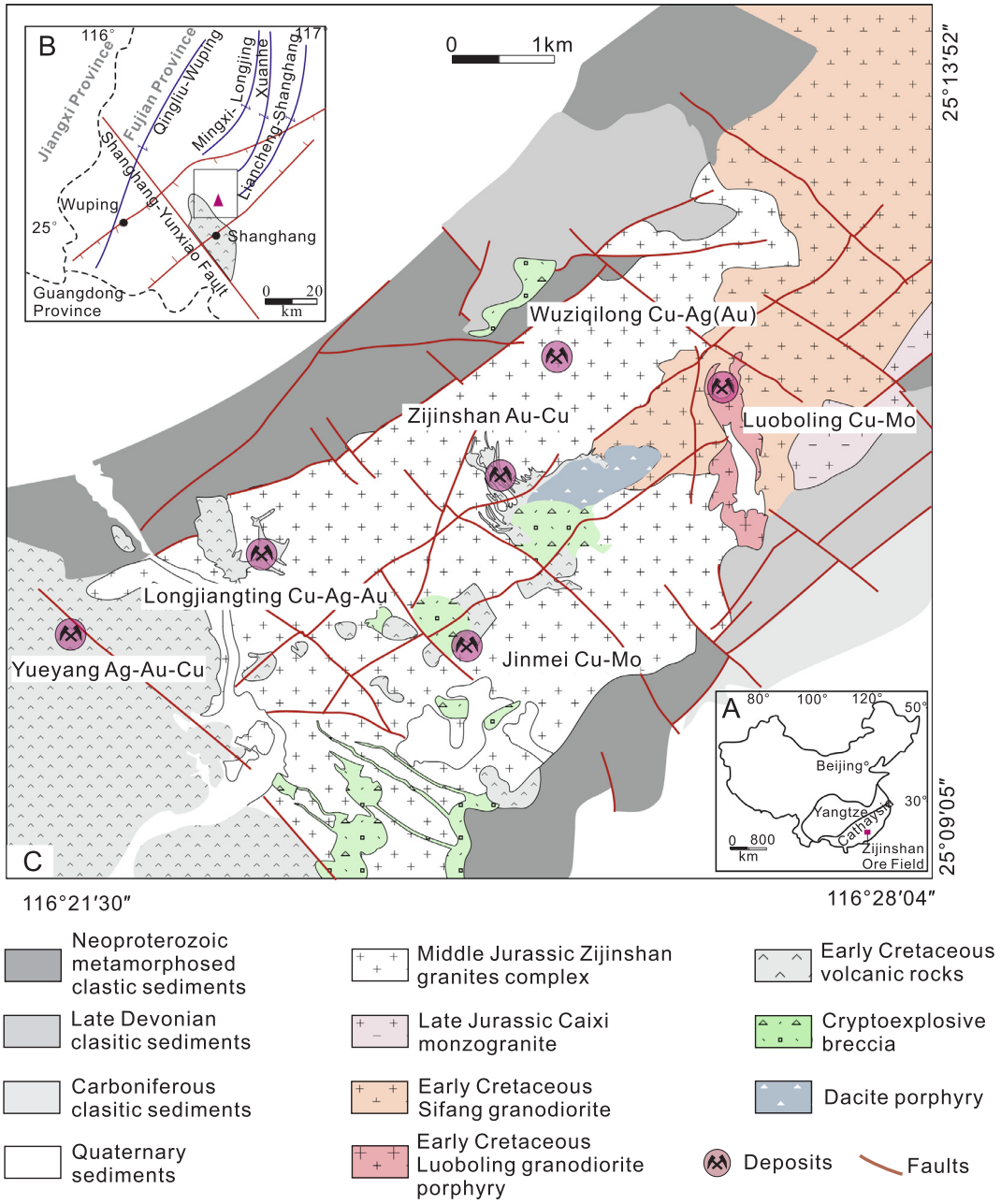

Fig. 1. (A) Map of China showing the traditional boundary of the Yangtze Carton and the Cathaysia Block (after Chen et al., 2008). (B) Map showing the regional tectonic framework of the Zijinshan region (after Jiang et al., 2013). (C) Geological map of the Zijinshan ore field (ZOF; modified after Jiang et al., 2013).

2007). The Sifang granodiorite crops out in the northeastern ZOF (Fig. 1) and has a zircon U-Pb age of 112 ± 1 Ma (Jiang et al., 2013). The Luoboling granodiorite porphyry associated with the Cu-Mo mineralization was emplaced into the Sifang granodiorite and yields a U-Pb age of 103.1 ± 1.1 Ma (Li and Jiang, 2014b). Recent dating of syenite and quartz-monzonite dikes, and the Zhongliao porphyritic granodiorite within the ZOF yielded zircon ages of 100–92 Ma (Wu et al., 2013; Li and Jiang, 2014a, 2014b).

2.1. Zijinshan high-sulfidation epithermal Au-Cu deposit

The Zijinshan HSE Au-Cu deposit is located in the central ZOF and is related to an early episode of Shimaoshan Group volcanism (So et al., 1998). It is the largest epithermal gold deposit in China and contains with 305 tons of gold at an average grade of ~1 g per ton (g/t) Au and 2.3 million tons of copper at an average grade of 0.36% Cu (Huang, 2008; Zhang, 2013).

The Zijinshan Au-Cu mineralization is closely spatially related with dacitic volcanic dome (Fig. 1, Fig. 2) and is generally hosted by cryptoexplosive breccia units (So et al., 1998; Zhang, 2013). These breccias are dominated by angular clasts in fine-grained and mineralized matrix. The clasts generally consist of altered Late Jurassic granites with some hydrothermal clasts (Fig. 3). The ore-hosting volcanic rocks have undergone pervasive hydrothermal alteration. For detailed reviews of the alteration zoning, see So et al. (1998) and Zhong et al. (2018). In brief, there are four zones between the shallow and central alteration zones, and the deeper alteration zones in the deposit (Fig. 2), namely (1) a silicic-alteration (Q) zone, (2) an alunite-alteration (Alu-Q) zone, (3) an either alunite alteration zone that overprints sericite-alteration (Q-Alu-Di-Phy; Zhong et al., 2018) or a dickite alteration zone (So et al., 1998), and (4) a sericite alteration (Phy) zone (Zhang et al., 1991, 2001, 2002, 2003, 2005; So et al., 1998; Zhong et al., 2018). The Q zone is located at

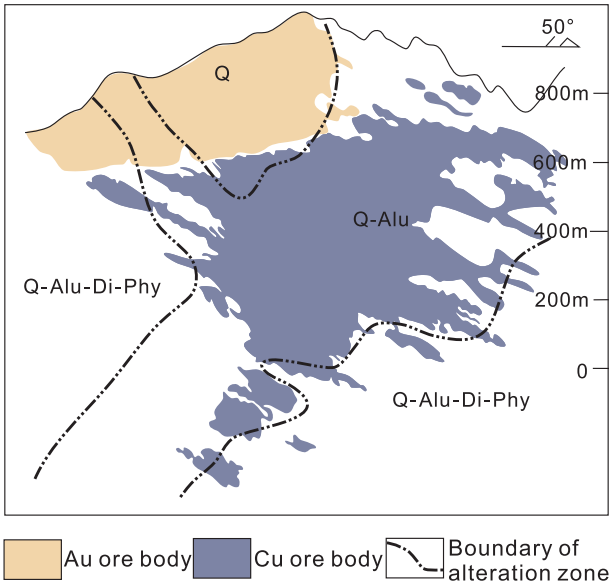

Fig. 2. Schematic cross section through the Zijinshan HSE Au-Cu deposit (modified after Zhang, 2013). Abbreviations are as follows: Q = silicic-alteration zone, Q-Alu (Di) = alunite alteration zone, and Q-Alu-Di-Phy = alunite-alteration zone overprinting sericite alteration.

altitude of > 650 m, contains quartz, opaline silica, limonite, goethite, dickite, and kaolinite, and is surrounded by gold orebodies that contain native gold and minor pyrite. The Alu-Q zone contains alunite, quartz, pyrite, and minor dickite and sericite, and is spatially associated with HSE copper mineralization. Ore minerals in the Alu-Q zone include covellite, digenite, and enargite, with minor chalcopyrite and bornite. The Phy zone contains sericite, quartz, and pyrite (So et al., 1998, Zhong et al., 2018), whereas the Q-Alu-Di-Phy zone contains quartz, alunite, dickite, sericite, and pyrite (Zhong et al., 2018). Some quartz-muscovite-dickite-pyrite veinlets occur in volcanic breccias within the Q-Alu-Di-Phy zone (Fig. 4). Alunite-dickite-quartz alteration occurs near the Ermiaogou Cu-(Au) deposit (Li et al., 2013) and the Longjiangting Cu-(Au) deposit (Chen et al., 2015) to the southwest of the Zijinshan HSE deposit (Fig. 5), indicating that this alunite alteration is widespread throughout the ZOF.

2.2. Luoboling porphyry Cu-Mo deposit

The Luoboling porphyry Cu-Mo deposit is located in the northeastern ZOF (Fig. 1C) and contains 1.4 million tons of Cu at an average grade of 0.3% and 110 thousand tons of Mo at an average grade of 0.036%. The Luoboling granodiorite porphyry consists of a series of small stocks with a surface area of 0.2 km^2 that were emplaced into the Sifang granodiorite and the Caixi monzogranite (Fig. 1C). Detailed geochronological research indicates the presence of two stages of mineralization-related granodiorite porphyry magmatism that yield zircon U-Pb ages of ca. 103 Ma and ca. 97 Ma (Huang et al., 2013; Li et al., 2017). They have similar mineral assemblages of plagioclase, quartz, biotite, and hornblende phenocrysts within a groundmass of quartz, K-feldspar, plagioclase, and biotite (Huang et al., 2013; Zhong et al., 2014). The barren Luoboling granodiorite is located at depths beneath the mineralization-related granodiorite porphyry (Fig. 6). The barren granodiorite has a similar mineral assemblage to the granodiorite porphyry but the latter contains more magnetite and hornblende (Zhong et al., 2014). For a detailed geological overview of the Luoboling porphyry deposit, see Zhong et al. (2014).

Previous research identified four main stages of hydrothermal alteration within the Luoboling porphyry deposit (Xie and Zhou, 1994; So et al., 1998; Zhang et al., 2001; Xue and Ni, 2008; Zhong et al., 2014) as follow. (1) Early potassic-silicic alteration formed K-feldspar, biotite, anhydrite, and magnetite within the porphyry. (2) Quartz-sericite alteration formed sericite, quartz, pyrite, and abundant quartz-sulfide veinlets and disseminated sulfides. This alteration was either generally peripheral or overprinted the earlier potassic-silicate alteration. (3) Propylitic alteration generated chlorite, epidote, and pyrite. This alteration locally overprints both potassic-silicic and quartz-sericite

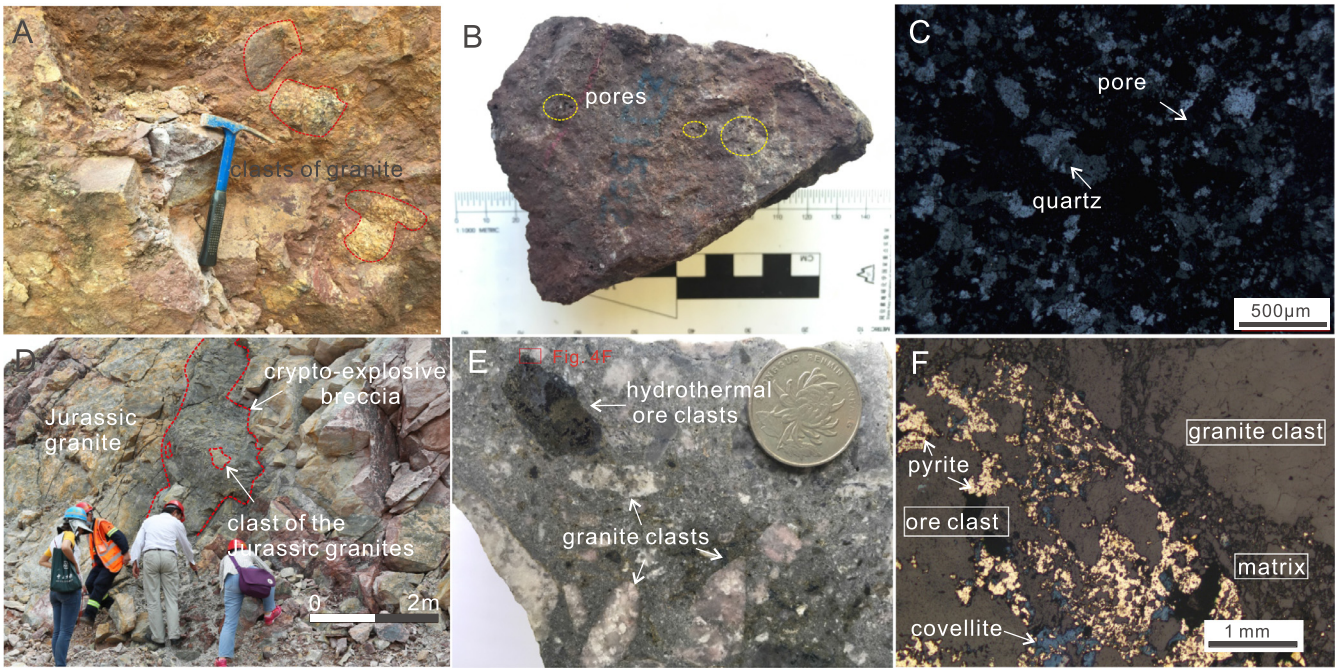

Fig. 3. Representative photographs and photomicrographs of samples from the study area. (A) Outcropping welded breccia. (B) Representative hand specimen of the welded breccia. (C) Transmitted light image showing a typical mineral assemblage within the welded breccia. (D) Field photograph of a crypto-explosive breccia. (E) Representative hand sample of the crypto-explosive breccia comprising clasts of hydrothermal mineralization and Jurassic granite. (F) Reflected light photomicrograph of the hand sample of crypto-explosive breccia in (E), showing the typical mineralogy of the hydrothermal ore clast within the breccia.

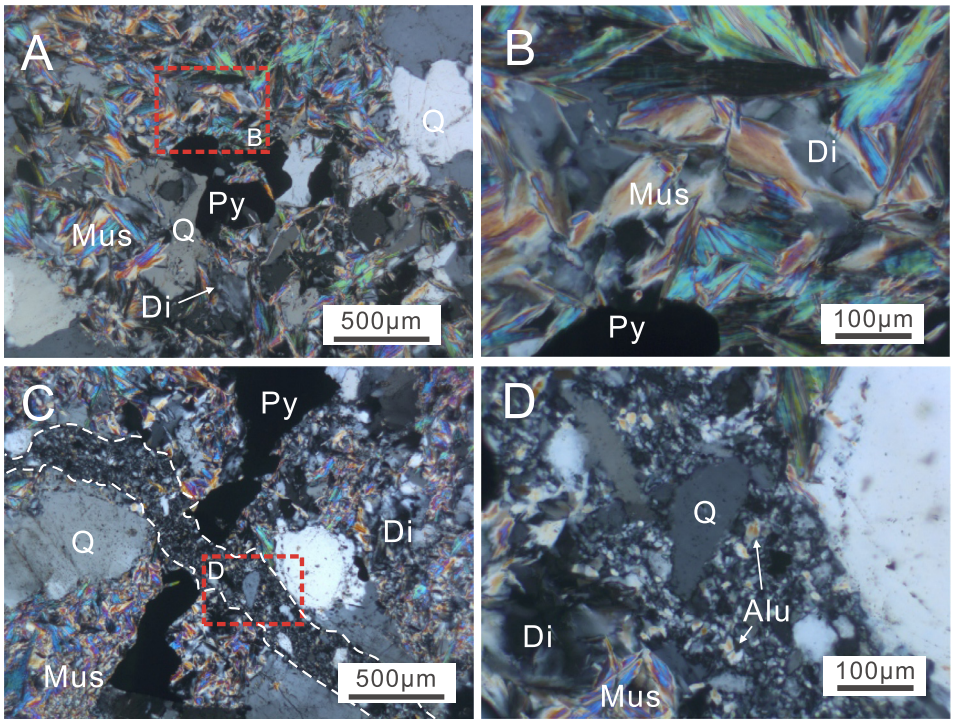

Fig. 4. Representative transmitted light photomicrographs of samples from the study area. (A) Quartz-muscovite-dickite-pyrite assemblage within the Zijinshan HSE Au-Cu deposit. (B) Higher-magnification view of planar crystal boundaries between muscovite and dickite. (C) Quartz-muscovite-dickite-pyrite assemblage cut by a quartz-alunite altered breccia. (D) Higher-magnification view of the quartz-alunite altered breccia. Abbreviations are as follows: Alu = alunite, Di = dickite, Mus = muscovite, Py = pyrite, and Q = quartz.

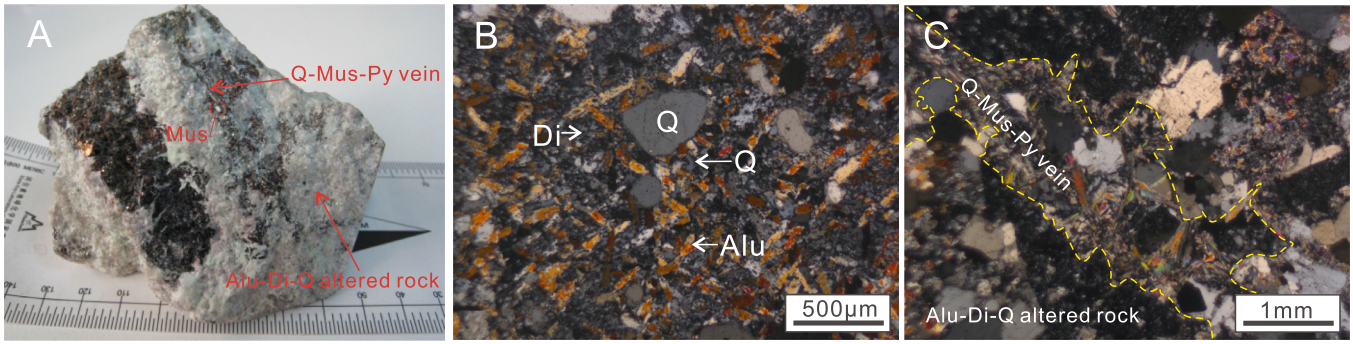

Fig. 5. (A) Photograph of a representative hand sample of the alunite-dickite alteration, cut by quartz-muscovite-pyrite vein. (B) Photomicrograph of a typical alunite-dickite alteration assemblage. (C) Photomicrograph of a quartz-muscovite-pyrite vein within the alunite-dickite alteration assemblage. Abbreviations are as in Fig. 4.

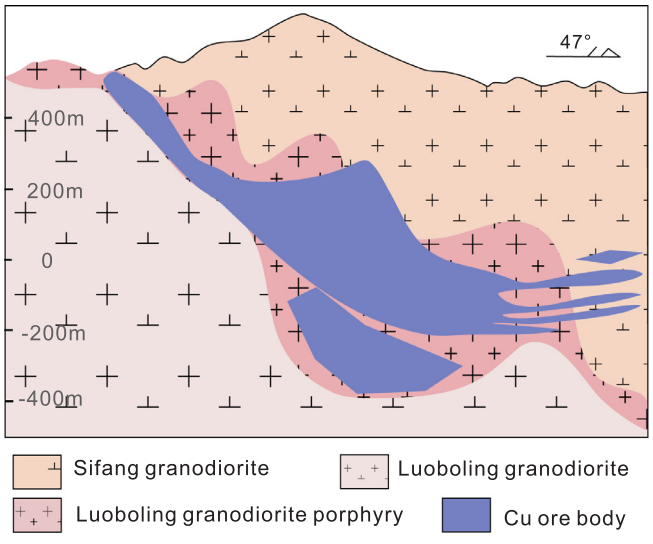

Fig. 6. Schematic cross section through the Luoboling porphyry Cu-Mo deposit (modified after Zhang, 2013).

alteration. (4) Argillic alteration formed hydromica, dickite, kaolinite, and quartz, spatially associated with pyrite, molybdenite and digenite mineralization. This alteration is generated located within the outer contact zone of the Luoboling granodiorite porphyry. The Luoboling Cu-Mo mineralization is generally hosted by veinlets or occurs as disseminated sulfides within those parts of the potassic-silicic alteration zone that are overprinted by quartz-sericite alteration. The deposit contains ore minerals of pyrite, chalcopyrite, and molybdenite, along with minor bornite, digenite, and magnetite.

3. Samples and analytical methods

3.1. Samples

Two muscovite samples were collected from the ZOF for Ar-Ar dating. Sample ZJ-27 was collected from a quartz-muscovite-dickite-pyrite veinlet (Fig. 4) at a depth of 320 m within drillhole ZK801 in the Q-Alu-Di-Phy zone of the Zijinshan HSE deposit. The second sample, LJ-04, was collected from an outcropping quartz-muscovite-pyrite veinlet (25°10′53.01″N, 116°23′19.4″E) that cuts an alunite-dickite altered rock (Fig. 5).

We obtained U-Pb ages and Lu-Hf isotopic compositions for zircons from (1) the matrix of a welded breccia within the lower Shimaoshan Formation, (2) the matrix of a HSE Au-Cu mineralized crypto-explosive breccia, and (3) the Luoboling granodiorite porphyry and the underlying barren granodiorite. The welded breccia (sample ZJ1502; 25°10′35.17″N, 116°24′12.58″E) is located directly above the Zijinshan granite complex (Fig. 3A) and comprises clasts of mainly Late Jurassic granite (Fig. 3A) in a matrix of rhyolitic tuff lavas (Fig. 3B, 3C). The crypto-explosive breccia (sample ZJ1505) was collected from an open pit associated with the Zijinshan HSE Au-Cu deposit (25°11′18.17″ N, 116°24′12.83″ E) and was emplaced within the fractures in the Zijinshan granite complex (Fig. 3D). The breccia contains clasts of Late Jurassic granite, volcanic rocks, and hydrothermal ore (Fig. 3E). The clasts of hydrothermal ore are dominated by pyrite and covellite (Fig. 3F), similar to the metallic mineral assemblage associated with the HSE Cu mineralization in this area. The breccia matrix is dominated by dacitic tuff material that records alunite, sericite, and pyrite alteration.

The samples of Luoboling granodiorite porphyry (LBL-82) and the underlying barren granodiorite (LBL-113) that were subjected to zircon U-Pb dating were obtained a depth of 680 m within drillhole ZK405 and from a depth of 825 m within drillhole ZK409, respectively. The Luoboling granodiorite porphyry contains biotite, plagioclase, quartz, and hornblende phenocrysts in a matrix of quartz, plagioclase, and K-feldspar. In comparison, the barren Luoboling granodiorite is phenocryst-free and contains plagioclase, hornblende, quartz, and K-feldspar.

3.2. Analytical methods

The muscovite subjected to Ar-Ar dating was handpicked from crushed samples of altered rocks from the Zijinshan deposit. Approximately 50 mg of muscovite was irradiated for 24 h in channel B4 of the Beijing 49–2 reactor at the Chinese Academy of Nuclear-Energy Sciences, Beijing, China. A ZBH-25 standard muscovite with an age of 132.7 Ma (Sang et al., 2006) was used to monitor neutron flux.

Total fusion analyses were undertaken using a GV Instrument 5400 mass spectrometer at the State Key Laboratory of Isotope Geochemistry, Guangzhou Institute of Geochemistry, Chinese Academy of Science, Guangzhou, China. Details of the analytical methods and data correction procedures are given by Qiu and Wijbrans (2006). Data processing was performed using the ArArCALC 2.4 software (Koppers, 2002), and $^{40}Ar/^{36}Ar$ versus $^{39}Ar/^{36}Ar$ isochron diagrams were constructed using Isoplot v. 4.0 software (Ludwig, 2003).

The zircon used for the U-Pb dating were separated from crushed and sieved samples (~1 kg) using standard density and magnetic separation techniques. Euhedral and clear zircons were then handpicked under a binocular microscope. More than 100 zircons were selected from each sample and were mounted in an epoxy resin for polishing prior to the LA analysis. Cathodoluminescence (CL) imaging was used to determine internal zircon structures prior to LA-ICP-MS analysis. Single zircons were analyzed by LA-ICP-MS, which allows simultaneous U-Pb dating and trace element analysis. For details of the U-Pb analysis, see Tu et al. (2011) and Zou et al. (2017). The analyses employed laser spots with a diameter of 31 μm, a constant repetition rate of 8 Hz, and a fluence of 8 J/cm^2. NIST SRM 610 glass (Pearce et al., 1997; Jochum et al., 2011) and Temora zircon (Black et al., 2003) standards were used for external standardization and were analyzed twice after every 5–10 analyses of unknowns. Analysis of the Temora zircon standard yielded a mean $^{206}Pb/^{238}U$ age of 416.83 ± 0.18 Ma (2σ, n = 52), agreeing well with the recommended $^{206}Pb/^{238}U$ age of 416.75 ± 0.24 Ma (2σ) (Black et al., 2003).

Off-line inspection and integration of both background and analytical signals, time-drift correction, and quantitative calibration of trace element and U-Pb data were performed using the ICPMSDataCal software package (Liu et al., 2010), and concordia diagrams and associated weighted means were calculated using the Isoplot v. 3.0 software package (Ludwig, 2003). Analyses with > 10% discordance in $^{206}Pb/^{238}U$ versus either $^{207}Pb/^{235}U$ or $^{208}Pb/^{232}Th$ at a level of one standard deviation (1σ) were not used in further age calculations (Liang et al., 2006). Cumulative probability plots were used to identify lead inheritance and/or loss. The main zircon populations usually yielded linear distributions with positive slopes, whereas outliers plotted above and below this line, representing zircons with inherited cores and lead loss, respectively. Both U-Pb ages and mean square weighted deviation (MSWD) values associated with the main zircon populations were obtained by removing outlying analyses. The resulting weighted mean $^{206}Pb/^{238}U$ ages for these main zircon populations were interpreted to represent the crystallization ages of the igneous rocks.

Zircon Lu-Hf isotopic analysis was undertaken using a Neptune multicollector (MC)-ICP-MS instrument coupled to a Resolution M-50 LA system. For details of the analytical and data correction procedures, see Wu et al. (2006). Repeat analysis of the Penglai zircon standard yielded a $^{176}Hf/^{177}Hf$ ratio of 0.282914 ± 0.000052 (2σ, n = 95), agreeing well with the recommended $^{176}Hf/^{177}Hf$ value of 0.282906 ± 0.000010 (2σ) (Li et al., 2010).

4. Results

4.1. Muscovite $^{40}Ar/^{39}Ar$ dating

Muscovite sample ZJ-27 from the Zijinshan HSE Au-Cu deposit yielded a flat age spectrum after stepwise laser heating. The main plateau consist of 16 successive steps (from steps 4 to 19) that represent 95.75% of the ^{39}Ar released, and yield a plateau age of 113.4 ± 1.1 Ma with a MSWD of 0.25 (Table 2; Fig. 7A). This apparent plateau age is consistent with the corresponding isochron age obtained for the main plateau from the Ar isotopic data (113.6 ± 1.2 Ma (2σ), MSWD of 0.25). The sample yields an initial $^{40}Ar/^{36}Ar$ value of 291 ± 14 (Fig. 7B), that is within uncertainty of the atmospheric argon value of 295.5 (Renne et al., 2009), indicating that the muscovite did not include inherited or excess ^{40}Ar. The plateau age of 113.4 ± 1.1 Ma therefore represents the crystallization age of the muscovite within this sample.

Removing the first and last few steps data for muscovite sample LJ-04 yielded a total of 17 successive steps (4 to 20) that represent 82.74% of ^{39}Ar released from the sample. These steps define the main plateau for this sample, yielding a plateau age of 110.4 ± 1.3 Ma with a MSWD of 0.12 (Fig. 7C). The Ar isotopic data for this main plateau yields a similar isochron age of 110.8 ± 1.5 Ma with a MSWD of 0.11 and an initial $^{40}Ar/^{36}Ar$ value of 292 ± 16 (Fig. 7D) that is within uncertainty of the atmospheric argon value of 295.5 (Renne et al., 2009), indicating that this muscovite does not include inherited or excess ^{40}Ar. The plateau age of 110.4 ± 1.3 Ma is therefore interpreted to represent the timing of crystallization of this muscovite.

4.2. Zircon LA-ICP-MS U-Pb ages

The zircons from the volcanic rocks associated with the Zijinshan Au-Cu deposit and from the Luoboling granodiorite porphyry and granodiorite contain well-developed oscillatory zoning (Fig. 8) that indicates a magmatic origin (Hoskin and Schaltegger, 2003).

Sample ZJ1502 is from the rhyolitic tuff matrix of the welded breccia and yields zircons that contain 94–324 ppm U and show Th/U ratios of 0.51–0.85. Thirty zircons from this sample yield U-Pb ages from 108.6 ± 1.4 to 120.3 ± 2.0 Ma and yield a weighted-mean zircon U-Pb age of 114.7 ± 0.9 Ma with a MSWD of 2.4 (Fig. 9A; Table 3).

Sample ZJ1505 is from the crypto-explosive breccia and yields zircon U-Pb ages from 108.5 to 630 Ma (Table 3). Two spots with U-Pb ages of 628 and 630 Ma represent inherited zircons, and a further seven zircons yield U-Pb ages of 137–167 Ma that may represent fragments derived from Jurassic granites. The remaining 10 zircons contain 363–1063 ppm U, have Th/U ratios of 0.18–0.68, and yield a mean U-

Table 2
Muscovite ^{40}Ar-^{39}Ar ages of representative samples from the Zijinshan high sulfidation epithermal deposit.

Sample No.	Step	Laser power (%)	$^{36}Ar_A$	$^{37}Ar_{Ca}$	$^{38}Ar_{Cl}$	$^{39}Ar_K$	$^{40}Ar^*$	Age	± 2σ	$^{40}Ar^*$	$^{39}Ar_k$	$^{39}Ar/^{36}Ar$	± 2σ	$^{40}Ar/^{36}Ar$	± 2σ
								(Ma)		(%)	(%)				
Zijinshan high-sulfidation epithermal Au-Cu deposit															
(a) ZJ-27	1	3.5%	14.934734	0.00	0.0000	174.2964	696.32	65.06	16.48	13.6	1.35	11.67	0.49	342.12	13.91
	2	3.7%	37.815952	0.00	0.0000	258.5695	225.09	14.38	28.88	2.0	2.00	6.84	0.29	301.45	12.24
	3	3.9%	1.800513	0.00	0.0350	115.5924	770.19	107.24	3.12	59.1	0.90	64.20	2.70	723.26	29.56
	4	4.1%	3.802768	0.00	0.0972	851.2065	6012.11	113.48	1.38	84.2	6.59	223.84	9.39	1876.48	76.47
	5	4.3%	3.914519	0.00	0.1880	869.9405	6140.24	113.41	1.40	84.1	6.74	222.23	9.44	1864.08	76.93
	6	4.5%	1.891660	0.00	0.2636	1099.6297	7785.81	113.75	1.15	93.2	8.51	581.30	24.67	4411.36	181.99
	7	4.7%	1.260654	21.67	0.1940	381.0819	2687.65	113.32	1.27	87.8	2.95	302.29	12.82	2427.45	100.00
	8	4.9%	0.911726	7.83	0.1793	507.1097	3576.65	113.33	1.16	92.9	3.93	556.21	23.57	4218.45	173.65
	9	5.1%	0.470439	0.60	0.2655	695.4940	4905.59	113.33	1.11	97.2	5.39	1478.39	64.23	10723.18	453.39
	10	5.3%	1.067684	4.04	0.0849	496.0686	3485.97	112.92	1.17	91.6	3.84	464.62	19.75	3560.48	147.09
	11	5.5%	0.578032	7.98	0.0831	733.6269	5201.74	113.91	1.12	96.7	5.68	1269.18	61.66	9294.56	441.92
	12	5.7%	0.234146	2.18	0.0784	289.3071	2047.46	113.70	1.12	96.7	2.24	1235.59	63.39	9039.87	454.91
	13	5.9%	0.040673	0.00	0.0113	56.7198	399.51	113.18	1.26	97.0	0.44	1394.53	237.10	10118.02	1717.15
	14	6.3%	0.373898	1.94	0.1741	751.7554	5328.20	113.87	1.11	97.9	5.82	2010.59	91.36	14545.92	644.77
	15	6.9%	0.111973	14.09	0.0766	247.8402	1753.20	113.65	1.12	98.1	1.92	2213.39	203.59	15952.83	1458.67
	16	7.9%	0.793998	13.63	0.4069	1441.9076	10167.91	113.31	1.10	97.7	11.16	1816.01	79.21	13101.48	556.22
	17	9.5%	0.419860	1.36	0.2127	706.1294	4976.50	113.24	1.11	97.5	5.47	1681.82	76.25	12148.25	537.13
	18	14.5%	1.283385	5.58	0.7052	2416.4950	17036.68	113.28	1.10	97.7	18.71	1882.91	79.51	13570.30	556.82
(b) LJ-04	1	3.1%	2.113491	8.93	0.0000	220.7770	1465.73	106.77	2.09	70.1	8.92	104.46	4.41	989.01	40.53
	2	3.3%	2.009749	0.22	0.0156	84.7324	515.54	98.09	4.68	46.4	3.43	42.16	1.80	552.02	22.95
	3	3.5%	0.840026	0.00	0.0948	75.2710	495.78	105.95	2.37	66.6	3.04	89.61	3.81	885.70	36.57
	4	3.7%	0.290781	0.61	0.0000	86.0145	592.44	110.65	1.27	87.3	3.48	295.81	13.23	2332.90	101.69
	5	3.9%	0.134294	0.00	0.0000	40.2817	276.90	110.44	1.50	87.4	1.63	299.95	20.38	2357.42	158.40
	6	4.1%	1.988803	0.00	0.1441	639.6690	4409.15	110.73	1.23	88.2	25.86	321.64	13.74	2512.49	104.38
	7	4.3%	0.453729	0.00	0.0204	115.2566	793.49	110.60	1.33	85.5	4.66	254.02	11.00	2044.31	86.12
	8	4.5%	0.483282	0.00	0.0574	115.9853	800.63	110.89	1.37	84.8	4.69	239.99	10.33	1952.15	81.75
	9	4.7%	0.503814	0.00	0.0503	93.3575	640.93	110.30	1.51	81.1	3.77	185.30	8.12	1567.66	66.87
	10	4.9%	0.075845	0.00	0.0000	16.4154	112.66	110.27	2.61	83.3	0.66	216.43	24.01	1780.86	196.68
	11	5.1%	0.588192	0.00	0.1374	110.5301	760.35	110.52	1.48	81.3	4.47	187.92	8.07	1588.19	66.32
	12	5.3%	0.169805	0.00	0.0000	15.2697	104.64	110.10	3.00	67.5	0.62	89.92	4.98	911.71	49.61
	13	5.5%	0.117652	0.00	0.0873	19.8798	136.87	110.60	2.11	79.7	0.80	168.97	11.20	1458.81	95.56
	14	5.7%	0.036605	0.00	0.0076	8.6284	59.35	110.50	3.39	84.5	0.35	235.72	37.89	1916.80	307.39
	15	5.9%	0.040068	0.00	0.0000	7.9519	54.48	110.07	3.74	82.1	0.32	198.46	30.15	1655.07	250.78
	16	6.3%	0.228289	0.00	0.0174	73.3226	503.47	110.32	1.29	88.1	2.96	321.18	16.19	2500.89	123.56
	17	6.9%	0.038782	0.00	0.0000	9.6178	66.03	110.31	3.55	85.1	0.39	248.00	44.43	1998.16	357.34
	18	7.9%	0.169269	0.00	0.0000	86.3608	592.93	110.31	1.19	92.1	3.49	510.20	29.63	3798.41	217.36
	19	9.5%	0.243542	0.00	0.0267	134.1101	927.16	111.05	1.16	92.7	5.42	550.67	28.10	4102.47	205.30
	20	14.5%	1.643553	0.00	0.3320	474.2669	3257.39	110.35	1.27	87.0	19.17	288.56	12.38	2277.42	94.98
	21	19.5%	0.720338	0.00	0.2048	42.8407	273.93	102.94	3.41	56.2	1.73	59.47	2.55	675.78	28.10
	22	30.0%	0.199021	1.39	0.0253	3.2888	17.06	83.96	15.10	22.5	0.13	16.53	0.97	381.23	20.15
	19	19.5%	3.742118	0.00	0.2009	821.9356	5776.43	112.93	1.39	83.9	6.36	219.64	9.21	1839.13	74.92

Pb age of 113.4 ± 1.9 Ma with a MSWD of 4.8. The large MSWD value for this age suggests that some of these zircons do not belong to the same age group as the others. The three zircons located at either end of the cumulative probability plot may have been undergone lead loss or inheritance, and are therefore excluded (Fig. 9B), leaving seven zircons that yield a U-Pb age for the crypto-explosive breccia of 112.9 ± 1.2 Ma with a MSWD of 0.96 (Fig. 9B).

The zircons from the Luoboling granodiorite porphyry (sample LBL-82) contain 479–1149 ppm U and have Th/U ratios of 0.32–0.64 (Table 3). Two zircons with U-Pb ages of 112.5 ± 2.4 and 95.8 ± 2.1 Ma within the cumulative probability plot (Fig. 9C) have undergone lead loss and lead inheritance, respectively, and are therefore excluded. The remaining 23 zircons yield U-Pb ages from 109.0 ± 2.4 to 102.0 ± 2.4 Ma and a mean U-Pb age of 103.8 ± 0.9 Ma (MSWD = 0.83).

The 25 analyses of zircons from the underlying barren granodiorite (sample LBL-113) yielded U contents of 276–3005 ppm and Th/U ratios of 0.19–0.82 (Table 3). Three zircons with U-Pb ages between 142.2 ± 4.0 Ma and 121.1 ± 3.2 Ma were most likely inherited from the Jurassic granites in this area. The remaining 22 zircons yielded ages between 101.5 ± 2.0 and 83.3 ± 1.7 Ma. Six of these zircons plot at either end of the cumulative probability plot, suggesting they have undergone either lead loss or lead inheritance (Fig. 9D). Excluding these spots yielded 16 zircons that produce a U-Pb age for the granodiorite of 98.1 ± 1.1 Ma (MSWD = 1.2).

4.3. Zircon Lu-Hf isotopic compositions

Zircons within the crypto-explosive breccia (sample ZJ1502) yield $^{176}Hf/^{177}Hf$ ratios of 0.282718–0.282661 and ε_{Hf} (t) values from −1.5 to 0.5 (calculated using the U-Pb crystallization age of each zircon; Table 4). These zircons have associated two-stage Hf model ages (T_{DM2}) of 1140 to 1268 Ma.

Zircons from the Luoboling granodiorite porphyry have $^{176}Hf/^{177}Hf$ ratios of 0.282583–0.282674, corresponding to ε_{Hf} (t) values from −4.5 to −1.2. Their two-stage Hf model ages range from 1214 to 1447 Ma.

Zircons from the Luoboling granodiorite have $^{176}Hf/^{177}Hf$ ratios of 0.282340–0.282592 and corresponding ε_{Hf} (t) values from −13.2 to −4.3, yielding two-stage Hf model ages between 1432 and 1994 Ma.

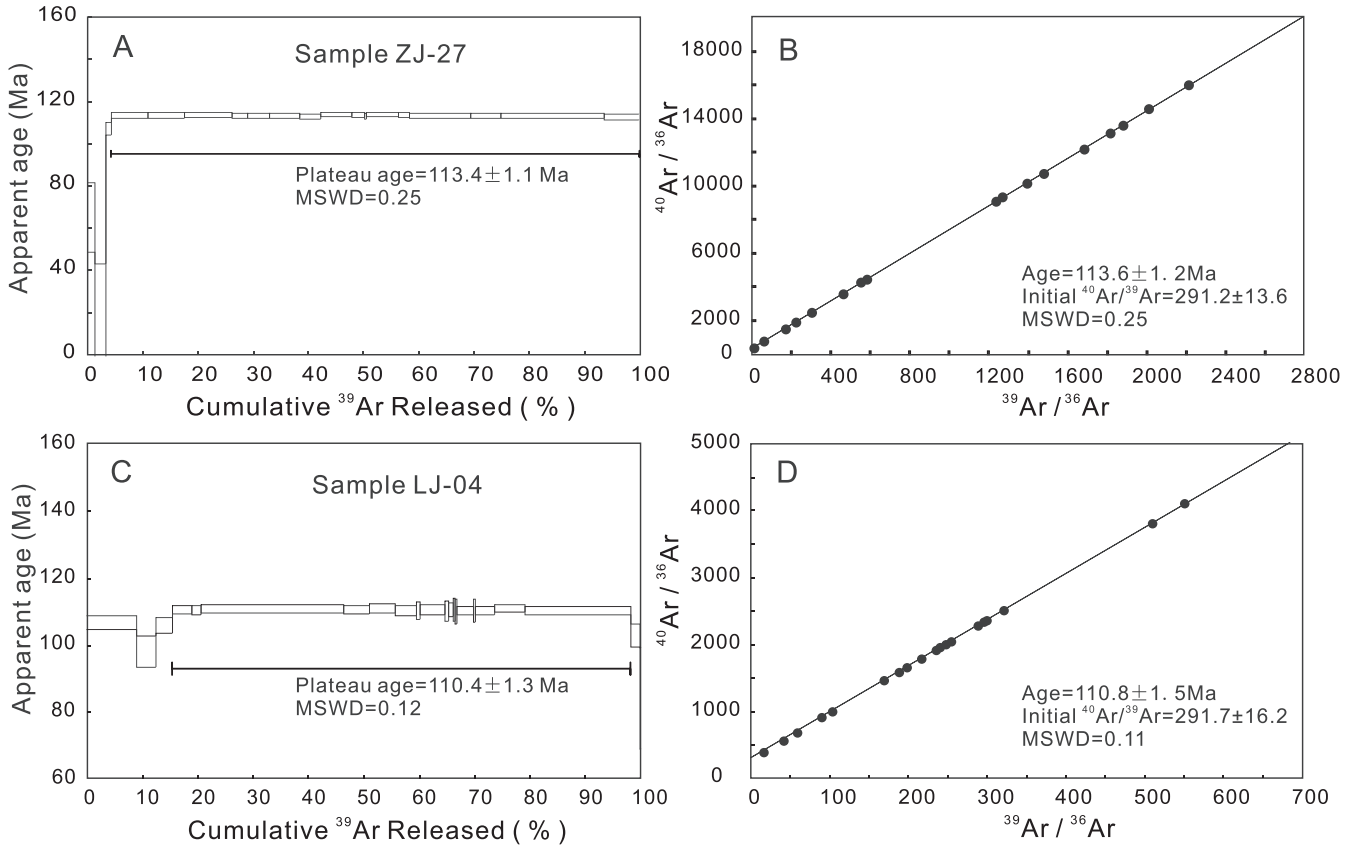

Fig. 7. Apparent muscovite ^{40}Ar-^{39}Ar ages (A and C) and associated isotopic correlation diagrams (B and D) for representative samples from the Zijinshan HSE Au-Cu deposit.

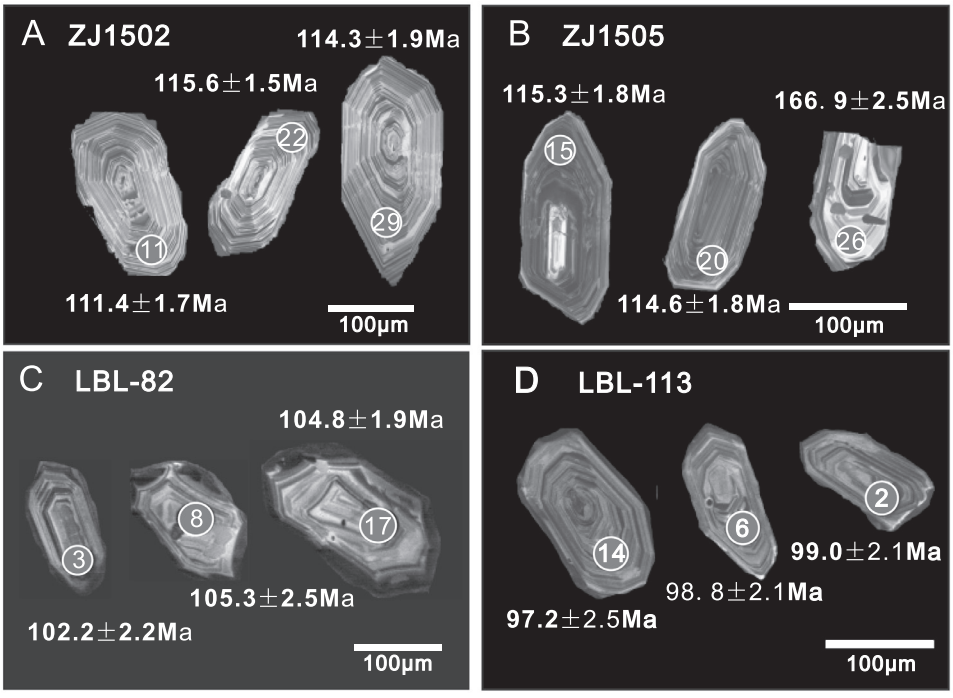

Fig. 8. CL images of representative zircons from (A) the welded breccia, (B) the crypto-explosive breccia associated with epithermal mineralization, (C) the Luoboling granodiorite porphyry, and (D) the underlying barren Luoboling granodiorite in the study area.

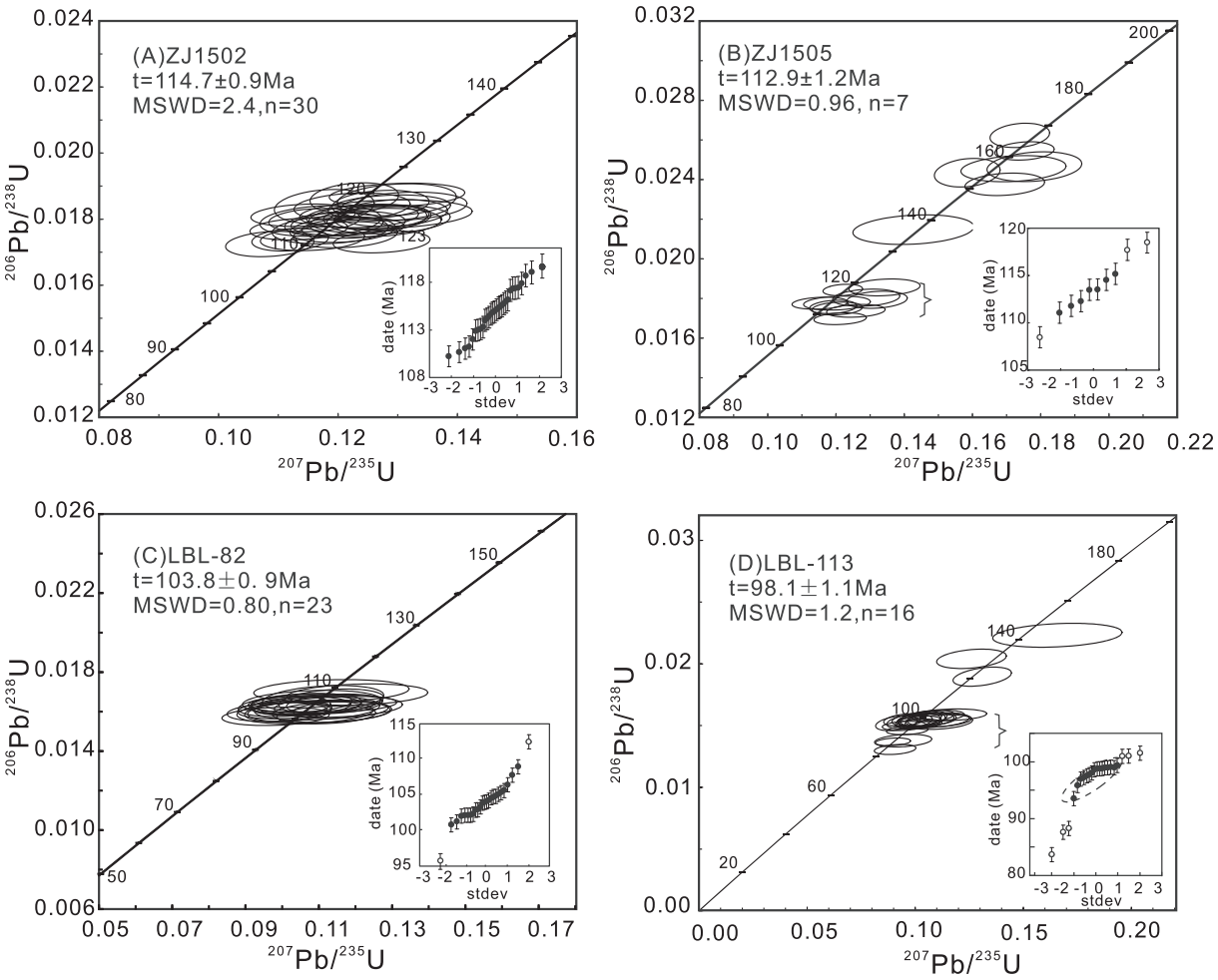

Fig. 9. Zircon U-Pb concordia diagrams for the zircon shown in Fig. 8: (A) Welded breccia; (B) Crypto-explosive breccia; (C) Luoboling granodiorite porphyry; and (D) Luoboling barren granodiorite. Insets show cumulative probability plots.

5. Discussion

5.1. Prolonged multi-phase Cretaceous magmatism within the Zijinshan orefield

The ZOF records several phases of Cretaceous magmatism (Fig. 10). For example, Zhang et al. (2001) reported Rb-Sr isochron ages of 125 ± 9.8 Ma for a basal dacite and 94.7 ± 7.7 Ma for a rhyolite at the top of the volcanic rocks of the Shimaoshan Group. However, these Rb-Sr dates may have been disturbed by later hydrothermal events (Cliff and Rickard, 1992). Recent researches have yielded more than 10 zircon U-Pb ages varying that range from 113 to 93 Ma for volcanic rocks within the ZOF (Hu et al., 2012; Xiao et al., 2012; Jiang et al., 2013; Fig. 10). Further zircon U-Pb ages from this area include ages of (1) ca. 112–107.8 Ma for the Sifang granodiorite (Mao et al., 2002; Yu et al., 2012; Jiang et al., 2013; Duan et al., 2017); (2) ca. 105–98.6 Ma for the Luoboling granodiorite porphyry (Huang et al., 2013; Duan et al., 2017; Li and Jiang, 2017); and (3) ca. 99.5–92.7 Ma for the Zhongliao granodiorite (Li and Jiang, 2014b) and the barren Luoboling granodiorite.

The new zircon U-Pb data of this study include an age of 114.7 ± 0.9 Ma for the welded breccia that immediately overlies the Late Jurassic granites and represents the earliest volcanic activity in the ZOF. This age, combined with the ages presented above, suggests that the Cretaceous magmatism in the ZOF spans the period from ca. 114.7 to 92 Ma (Hu et al., 2012; Xiao et al., 2012; Jiang et al., 2013; Fig. 10).

Previously reported ages for the Zijinshan HSE deposit were derived from low-temperature alteration minerals and fluid inclusions using K-Ar and Rb-Sr methods, respectively (Zhang et al., 1991, 2005; Chen, 1996; Zhou and Chen, 1996; Mao et al., 2002). These ages span a wide range from 124 to 82 Ma, indicating that the prolonged and multi-phase magmatism within the ZOF could have disturbed the K-Ar isotope systems within alunite and adularia, both of which have relatively low closure temperatures (130 °C–150 °C and 210 °C–200 °C, respectively; Harrison and McDougall, 1982; Snee, 2002).

5.2. Asynchronous formation of porphyry and epithermal mineralization within the ZOF

Previous geochronological analysis of the Zijinshan deposit yielded four K-Ar ages on alunite from 82 to 111.7 Ma (Zhou and Chen, 1996; Zhang et al., 2005), two Rb-Sr isochron ages on quartz-hosted fluid inclusions of 100 and 122 Ma (Zhou and Chen, 1996), and three Rb-Sr isochron ages on whole-rock samples from 110 to 124 Ma (Chen, 1996; Mao et al., 2002). The large range of these ages (from 124 to 82 Ma) suggests that both the alunite K-Ar system, which has a closure temperature of 130 °C–150 °C (Harrison and Mcdougall, 1982), and the Rb-Sr system within these samples were disturbed by later hydrothermal events within the ZOF. Jiang et al. (2017) reported a Re-Os isochron age of 103 ± 4 Ma for pyrite from the Zijinshan deposit, although this age has a very large MSWD (2 2 2) as well as Re-Os model ages that range from 142 to 82 Ma (Jiang et al., 2017). This indicates that these pyrites formed over several stages of hydrothermal activity (Cardon et al., 2008; Li et al., 2018).

Table 3
Zircon U-Th-Pb isotopic data of igneous rocks from the Zijinshan orefield.

Analysis	Pb	U	Th/U	Atomic Ratios								rho	Ages(Ma)						Concordance
	(ppm)			$^{206}Pb/^{238}U$	± 1σ	$^{207}Pb/^{235}U$	± 1σ	$^{207}Pb/^{206}Pb$	± 1σ	$^{208}Pb/^{232}Th$	± 1σ		$^{207}Pb/^{235}U$	± 1σ	$^{208}Pb/^{232}Th$	± 1σ	$^{206}Pb/^{238}U$	± 1σ	
Welded breccia																			
ZJ1502-01	5.9	163	0.63	0.01732	0.00026	0.11892	0.00659	0.04940	0.00275	0.00531	0.00019	0.27	114.1	6.0	107.0	3.8	110.7	1.6	96%
ZJ1502-02	7.6	233	0.70	0.01728	0.00026	0.11635	0.00536	0.04856	0.00221	0.00527	0.00017	0.33	111.8	4.9	106.2	3.4	110.4	1.6	98%
ZJ1502-03	7.3	257	0.81	0.01703	0.00022	0.12291	0.00507	0.05215	0.00221	0.00506	0.00016	0.31	117.7	4.6	102.1	3.2	108.8	1.4	92%
ZJ1502-04	7.4	207	0.63	0.01752	0.00021	0.12048	0.00534	0.04978	0.00231	0.00537	0.00016	0.27	115.5	4.8	108.2	3.2	112.0	1.3	96%
ZJ1502-05	9.7	297	0.69	0.01749	0.00022	0.11298	0.00486	0.04665	0.00200	0.00555	0.00016	0.29	108.7	4.4	111.8	3.2	111.8	1.4	97%
ZJ1502-06	5.8	153	0.59	0.01816	0.00025	0.12478	0.00616	0.04994	0.00255	0.00566	0.00018	0.28	119.4	5.6	114.1	3.7	116.0	1.6	97%
ZJ1502-07	6.0	140	0.54	0.01850	0.00025	0.12714	0.00680	0.04988	0.00271	0.00638	0.00022	0.25	121.5	6.1	128.5	4.4	118.2	1.6	97%
ZJ1502-08	7.1	189	0.60	0.01823	0.00033	0.11558	0.00515	0.04608	0.00200	0.00599	0.00020	0.41	111.1	4.7	120.7	4.1	116.4	2.1	95%
ZJ1502-09	4.9	116	0.54	0.01802	0.00029	0.12895	0.00631	0.05198	0.00254	0.00614	0.00021	0.33	123.2	5.7	123.7	4.1	115.1	1.9	93%
ZJ1502-10	6.5	164	0.56	0.01761	0.00025	0.11773	0.00524	0.04842	0.00218	0.00568	0.00016	0.32	113.0	4.8	114.5	3.3	112.5	1.6	99%
ZJ1502-11	6.2	157	0.55	0.01743	0.00027	0.11941	0.00601	0.05008	0.00253	0.00539	0.00017	0.31	114.5	5.4	108.6	3.4	111.4	1.7	97%
ZJ1502-12	6.9	173	0.57	0.01817	0.00028	0.12455	0.00623	0.04968	0.00247	0.00554	0.00019	0.31	119.2	5.6	111.7	3.8	116.1	1.8	97%
ZJ1502-13	7.4	203	0.66	0.01825	0.00026	0.12984	0.00579	0.05147	0.00226	0.00580	0.00019	0.32	124.0	5.2	117.0	3.8	116.6	1.6	93%
ZJ1502-14	6.8	152	0.51	0.01806	0.00023	0.12467	0.00599	0.05020	0.00250	0.00576	0.00019	0.26	119.3	5.4	116.0	3.9	115.4	1.5	96%
ZJ1502-15	10.2	303	0.67	0.01744	0.00023	0.11761	0.00535	0.04885	0.00220	0.00527	0.00016	0.29	112.9	4.9	106.2	3.3	111.4	1.5	98%
ZJ1502-16	7.8	289	0.91	0.01784	0.00030	0.11824	0.00649	0.04846	0.00269	0.00530	0.00017	0.31	113.5	5.9	106.9	3.4	114.0	1.9	99%
ZJ1502-17	8.0	210	0.58	0.01739	0.00023	0.11752	0.00553	0.04941	0.00241	0.00546	0.00018	0.29	112.8	5.0	110.0	3.6	111.1	1.5	98%
ZJ1502-18	4.1	94	0.52	0.01824	0.00028	0.12769	0.00928	0.05053	0.00353	0.00576	0.00024	0.21	122.0	8.4	116.1	4.8	116.6	1.8	95%
ZJ1502-19	9.3	236	0.60	0.01850	0.00029	0.13048	0.00531	0.05159	0.00209	0.00584	0.00017	0.38	124.5	4.8	117.7	3.4	118.2	1.8	94%
ZJ1502-20	6.2	168	0.64	0.01799	0.00024	0.13082	0.00610	0.05307	0.00253	0.00582	0.00019	0.28	124.8	5.5	117.3	3.8	114.9	1.5	91%
ZJ1502-21	7.3	178	0.61	0.01884	0.00031	0.13914	0.00739	0.05429	0.00287	0.00667	0.00020	0.31	132.3	6.6	134.4	4.0	120.3	2.0	90%
ZJ1502-22	7.7	172	0.51	0.01810	0.00024	0.13149	0.00521	0.05284	0.00205	0.00589	0.00019	0.34	125.4	4.7	118.7	3.8	115.6	1.5	91%
ZJ1502-23	8.2	243	0.68	0.01761	0.00023	0.11214	0.00438	0.04621	0.00177	0.00553	0.00015	0.34	107.9	4.0	111.5	3.0	112.5	1.5	95%
ZJ1502-24	8.1	245	0.67	0.01698	0.00022	0.11336	0.00402	0.04862	0.00175	0.00514	0.00015	0.36	109.0	3.7	103.6	3.0	108.6	1.4	99%
ZJ1502-25	5.2	147	0.71	0.01866	0.00033	0.12958	0.00636	0.05099	0.00270	0.00643	0.00020	0.36	123.7	5.7	129.5	4.0	119.2	2.1	96%
ZJ1502-26	8.3	250	0.67	0.01688	0.00023	0.10632	0.00445	0.04589	0.00197	0.00519	0.00016	0.33	102.6	4.1	104.5	3.1	107.9	1.5	94%
ZJ1502-27	7.5	237	0.71	0.01731	0.00024	0.11632	0.00549	0.04870	0.00223	0.00517	0.00015	0.29	111.7	5.0	104.3	3.0	110.6	1.5	99%
ZJ1502-28	9.1	299	0.78	0.01776	0.00022	0.11232	0.00532	0.04582	0.00214	0.00565	0.00016	0.27	108.1	4.9	114.0	3.2	113.5	1.4	95%
ZJ1502-29	9.1	324	0.85	0.01790	0.00030	0.11815	0.00482	0.04753	0.00171	0.00567	0.00017	0.41	113.4	4.4	114.3	3.5	114.4	1.9	99%
ZJ1502-30	6.1	174	0.65	0.01803	0.00027	0.11605	0.00605	0.04666	0.00242	0.00568	0.00020	0.29	111.5	5.5	114.4	3.9	115.2	1.7	96%
Crypto-explosive breccia																			
ZJ1505-01	3.8	99	1.57	0.02455	0.00044	0.17201	0.01017	0.05135	0.00319	0.00695	0.00022	0.30	161.2	8.8	140.0	4.5	156.4	2.7	96%
ZJ1505-02	6.5	215	0.58	0.02376	0.00037	0.16945	0.00771	0.05219	0.00247	0.00734	0.00024	0.35	158.9	6.7	147.8	4.7	151.4	2.4	95%
ZJ1505-03	34.7	293	0.11	0.10253	0.00193	0.98274	0.02703	0.06935	0.00146	0.03691	0.00133	0.69	695.0	13.8	732.6	26.0	629.2	11.3	90%
ZJ1505-04	10.1	506	0.20	0.01749	0.00021	0.12036	0.00489	0.04979	0.00194	0.00600	0.00030	0.30	115.4	4.4	120.9	6.1	111.8	1.4	96%
ZJ1505-05	8.4	363	0.68	0.01777	0.00023	0.12030	0.00646	0.04930	0.00270	0.00555	0.00019	0.24	115.3	5.9	111.9	3.9	113.5	1.5	98%
ZJ1505-06	1.6	62	0.50	0.02147	0.00049	0.14268	0.01170	0.04859	0.00390	0.00668	0.00036	0.28	135.4	10.4	134.6	7.2	137.0	3.1	98%
ZJ1505-07	16.0	462	0.58	0.02889	0.00062	0.23251	0.00753	0.06025	0.00272	0.00860	0.00034	0.66	212.3	6.2	173.1	6.8	183.6	3.9	85%
ZJ1505-08	23.7	1063	0.36	0.01843	0.00019	0.12200	0.00384	0.04795	0.00150	0.00567	0.00018	0.33	116.9	3.5	114.2	3.6	117.7	1.2	99%
ZJ1505-09	16.1	748	0.37	0.01738	0.00021	0.12582	0.00568	0.05252	0.00244	0.00580	0.00019	0.27	120.3	5.1	116.8	3.7	111.1	1.3	91%
ZJ1505-10	9.6	465	0.31	0.01560	0.00018	0.16554	0.00906	0.07717	0.00447	0.00825	0.00047	0.21	155.5	7.9	166.1	9.4	99.8	1.1	56%
ZJ1505-11	11.8	579	0.23	0.01698	0.00020	0.12123	0.00507	0.05159	0.00215	0.00624	0.00023	0.28	116.2	4.6	125.8	4.5	108.5	1.3	93%
ZJ1505-12	8.4	292	0.97	0.01806	0.00049	0.24612	0.01280	0.10134	0.00588	0.00836	0.00030	0.53	223.4	10.4	168.3	6.1	115.4	3.1	36%
ZJ1505-13	12.2	571	0.32	0.01652	0.00026	0.19326	0.01082	0.08414	0.00453	0.00858	0.00047	0.28	179.4	9.2	172.6	9.5	105.7	1.7	48%
ZJ1505-14	9.4	437	0.18	0.01856	0.00028	0.13422	0.00688	0.05208	0.00257	0.00675	0.00028	0.30	127.9	6.2	136.0	5.6	118.5	1.8	92%
ZJ1505-15	10.6	507	0.22	0.01804	0.00028	0.12887	0.00649	0.05153	0.00255	0.00614	0.00029	0.31	123.1	5.8	123.7	5.9	115.3	1.8	93%
ZJ1505-16	7.3	238	0.52	0.02465	0.00049	0.17815	0.00917	0.05216	0.00261	0.00821	0.00037	0.39	166.5	7.9	165.3	7.5	157.0	3.1	94%
ZJ1505-17	75.4	245	0.18	0.27189	0.00727	4.98331	0.20387	0.13190	0.00426	0.07905	0.00325	0.65	1816.5	34.6	1537.7	60.9	1550.4	36.8	84%
ZJ1505-18	10.7	577	0.28	0.01552	0.00020	0.12634	0.00593	0.05867	0.00270	0.00557	0.00023	0.28	120.8	5.3	112.3	4.6	99.3	1.3	80%
ZJ1505-19	10.0	424	0.32	0.01647	0.00030	0.24927	0.01834	0.10936	0.00736	0.01149	0.00089	0.25	226.0	14.9	230.8	17.8	105.3	1.9	27%
ZJ1505-20	12.2	584	0.22	0.01793	0.00028	0.13200	0.00587	0.05358	0.00246	0.00648	0.00025	0.36	125.9	5.3	130.6	5.1	114.6	1.8	90%

(*continued on next page*)

Table 3 (*continued*)

Analysis	Pb	U	Th/U	Atomic Ratios								rho	Ages(Ma)						Concordance
	(ppm)			$^{206}Pb/^{238}U$	± 1σ	$^{207}Pb/^{235}U$	± 1σ	$^{207}Pb/^{206}Pb$	± 1σ	$^{208}Pb/^{232}Th$	± 1σ		$^{207}Pb/^{235}U$	± 1σ	$^{208}Pb/^{232}Th$	± 1σ	$^{206}Pb/^{238}U$	± 1σ	
ZJ1505-21	12.7	588	0.43	0.01776	0.00020	0.11529	0.00541	0.04691	0.00216	0.00534	0.00016	0.24	110.8	4.9	107.6	3.3	113.5	1.3	97%
ZJ1505-22	13.0	437	0.53	0.02435	0.00048	0.15847	0.00636	0.04690	0.00162	0.00918	0.00033	0.49	149.4	5.6	184.7	6.7	155.1	3.0	96%
ZJ1505-23	13.7	631	1.07	0.01443	0.00021	0.28290	0.02225	0.14348	0.01293	0.00550	0.00038	0.19	253.0	17.6	110.8	7.7	92.4	1.3	6%
ZJ1505-24	8.1	199	0.12	0.03445	0.00052	0.37422	0.01451	0.07885	0.00295	0.02390	0.00107	0.39	322.8	10.7	477.4	21.2	218.3	3.3	61%
ZJ1505-25	18.3	614	0.32	0.02545	0.00031	0.17524	0.00575	0.04987	0.00156	0.00795	0.00023	0.37	164.0	5.0	160.0	4.6	162.0	1.9	98%
ZJ1505-26	23.4	782	0.26	0.02623	0.00041	0.17387	0.00576	0.04820	0.00158	0.00831	0.00025	0.47	162.8	5.0	167.2	5.0	166.9	2.5	97%
ZJ1505-27	7.7	193	0.55	0.02495	0.00035	0.47538	0.02656	0.13859	0.00781	0.01703	0.00069	0.25	394.9	18.3	341.3	13.7	158.9	2.2	14%
ZJ1505-28	11.6	563	0.29	0.01757	0.00022	0.11916	0.00456	0.04927	0.00190	0.00612	0.00021	0.33	114.3	4.1	123.3	4.3	112.3	1.4	98%
ZJ1505-29	9.3	440	0.34	0.01776	0.00028	0.13490	0.00672	0.05581	0.00297	0.00625	0.00032	0.31	128.5	6.0	125.9	6.3	113.5	1.8	87%
ZJ1505-30	32.5	263	0.59	0.10237	0.00192	0.90757	0.02899	0.06431	0.00179	0.02825	0.00104	0.59	655.8	15.4	563.0	20.5	628.3	11.2	95%
Luoboling granodiorite porphyry																			
LBL-82-01	13.2	697	0.54	0.00036	0.23490	0.10656	0.01007	0.04761	0.00429	0.00531	0.00030	0.23	102.8	9.2	107.1	6.1	104.6	2.3	98%
LBL-82-02	15.2	805	0.42	0.00031	0.22268	0.10508	0.00898	0.04654	0.00385	0.00503	0.00025	0.22	101.5	8.2	101.4	5.0	104.1	2.0	97%
LBL-82-03	10.2	557	0.42	0.00035	0.23327	0.11340	0.01060	0.05188	0.00475	0.00504	0.00027	0.23	109.1	9.7	101.5	5.4	102.2	2.2	93%
LBL-82-04	10.2	551	0.37	0.00032	0.22688	0.10749	0.00923	0.04784	0.00414	0.00531	0.00035	0.23	103.7	8.5	107.0	7.0	104.2	2.0	99%
LBL-82-05	9.8	519	0.40	0.00044	0.26878	0.11118	0.01094	0.04931	0.00532	0.00516	0.00034	0.27	107.0	10.0	104.0	6.8	106.5	2.8	99%
LBL-82-06	13.7	723	0.57	0.00030	0.22152	0.10070	0.00849	0.04526	0.00387	0.00525	0.00028	0.22	97.4	7.8	105.9	5.6	102.9	1.9	94%
LBL-82-07	12.0	625	0.54	0.00034	0.25307	0.10063	0.00831	0.04499	0.00390	0.00542	0.00032	0.25	97.4	7.7	109.3	6.4	104.0	2.2	93%
LBL-82-08	9.7	508	0.48	0.00040	0.20820	0.10802	0.01244	0.04709	0.00532	0.00555	0.00041	0.21	104.2	11.4	111.8	8.3	105.3	2.5	98%
LBL-82-09	11.4	615	0.42	0.00032	0.26389	0.10159	0.00779	0.04632	0.00387	0.00579	0.00032	0.26	98.2	7.2	116.8	6.4	102.1	2.1	96%
LBL-82-10	13.2	733	0.40	0.00032	0.21680	0.09862	0.00900	0.04408	0.00377	0.00506	0.00029	0.22	95.5	8.3	101.9	5.8	102.2	2.0	93%
LBL-82-11	12.3	655	0.53	0.00039	0.20536	0.11026	0.01298	0.05049	0.00590	0.00566	0.00034	0.21	106.2	11.9	114.1	6.8	102.3	2.5	96%
LBL-82-12	14.4	780	0.47	0.00030	0.23444	0.11205	0.00892	0.05055	0.00408	0.00511	0.00027	0.23	107.8	8.1	103.0	5.4	101.2	1.9	93%
LBL-82-13	12.9	665	0.64	0.00041	0.29581	0.11341	0.00944	0.04966	0.00414	0.00501	0.00024	0.30	109.1	8.6	101.1	4.7	105.6	2.6	96%
LBL-82-14	10.2	519	0.49	0.00038	0.17995	0.11346	0.01400	0.04867	0.00612	0.00539	0.00031	0.18	109.1	12.8	108.6	6.3	109.0	2.4	99%
LBL-82-15	10.5	559	0.46	0.00035	0.21477	0.11534	0.01155	0.05208	0.00549	0.00546	0.00031	0.21	110.8	10.5	110.1	6.2	103.9	2.2	93%
LBL-82-16	10.2	546	0.52	0.00038	0.20722	0.10626	0.01229	0.04774	0.00545	0.00510	0.00029	0.21	102.5	11.3	102.9	5.9	102.0	2.4	99%
LBL-82-17	10.4	539	0.56	0.00030	0.15416	0.11099	0.01338	0.04870	0.00576	0.00547	0.00033	0.15	106.9	12.2	110.3	6.7	104.8	1.9	98%
LBL-82-18	13.0	629	0.54	0.00039	0.21459	0.12491	0.01274	0.05142	0.00521	0.00547	0.00026	0.21	119.5	11.5	110.2	5.2	112.5	2.4	93%
LBL-82-19	10.6	573	0.37	0.00031	0.21778	0.10534	0.00913	0.04696	0.00419	0.00481	0.00028	0.22	101.7	8.4	97.0	5.6	105.1	2.0	96%
LBL-82-20	13.4	670	0.56	0.00036	0.20016	0.12054	0.01269	0.05249	0.00558	0.00525	0.00026	0.20	115.6	11.5	105.8	5.3	107.8	2.3	93%
LBL-82-21	12.8	668	0.41	0.00029	0.24690	0.11603	0.00854	0.05261	0.00383	0.00531	0.00030	0.25	111.5	7.8	107.0	6.0	102.9	1.9	92%
LBL-82-22	9.0	479	0.44	0.00039	0.23427	0.10953	0.01129	0.05162	0.00552	0.00494	0.00033	0.23	105.5	10.3	99.6	6.6	103.3	2.5	97%
LBL-82-23	19.4	1149	0.31	0.00033	0.29956	0.09836	0.00728	0.04722	0.00328	0.00485	0.00024	0.30	95.3	6.7	97.9	4.7	95.8	2.1	99%
LBL-82-24	13.1	684	0.57	0.00031	0.19724	0.09823	0.00967	0.04564	0.00464	0.00501	0.00024	0.20	95.1	8.9	101.1	4.8	100.8	1.9	94%
LBL-82-25	13.5	702	0.44	0.00033	0.26431	0.11428	0.00865	0.05059	0.00389	0.00515	0.00027	0.26	109.9	7.9	103.9	5.5	104.8	2.1	95%
Barren Luoboling granodiorite																			
LBL-113-01	7.1	276	0.45	0.02231	0.00064	0.16584	0.01977	0.05288	0.00598	0.00763	0.00057	0.24	155.8	17.2	153.6	11.4	142.2	4.0	90%
LBL-113-02	26.2	1532	0.29	0.01548	0.00033	0.10780	0.00743	0.05027	0.00347	0.00567	0.00029	0.31	104.0	6.8	114.2	5.9	99.0	2.1	95%
LBL-113-03	27.7	1365	0.88	0.01578	0.00030	0.10841	0.00635	0.04958	0.00291	0.00530	0.00023	0.32	104.5	5.8	106.8	4.5	100.9	1.9	96%
LBL-113-04	30.0	1971	0.28	0.01368	0.00020	0.08974	0.00536	0.04737	0.00282	0.00525	0.00022	0.25	87.3	5.0	105.8	4.4	87.6	1.3	99%
LBL-113-05	40.9	2221	0.68	0.01545	0.00033	0.09518	0.00643	0.04464	0.00289	0.00508	0.00021	0.32	92.3	6.0	102.3	4.2	98.8	2.1	93%
LBL-113-06	22.7	1384	0.19	0.01544	0.00033	0.10173	0.00655	0.04762	0.00289	0.00556	0.00031	0.34	98.4	6.0	112.1	6.1	98.8	2.1	99%
LBL-113-07	25.5	1522	0.30	0.01532	0.00039	0.09743	0.00696	0.04603	0.00316	0.00538	0.00023	0.36	94.4	6.4	108.4	4.7	98.0	2.5	96%
LBL-113-08	14.8	747	0.80	0.01579	0.00030	0.11050	0.00804	0.05024	0.00347	0.00510	0.00022	0.26	106.4	7.3	102.8	4.4	101.0	1.9	94%
LBL-113-09	32.3	2033	0.15	0.01548	0.00044	0.10230	0.00657	0.04852	0.00311	0.00546	0.00032	0.44	98.9	6.1	110.1	6.5	99.0	2.8	99%
LBL-113-10	18.8	828	0.59	0.01896	0.00051	0.13104	0.00893	0.05021	0.00330	0.00594	0.00029	0.40	125.0	8.0	119.8	5.9	121.1	3.2	96%
LBL-113-11	50.6	3005	0.27	0.01514	0.00025	0.10191	0.00695	0.04833	0.00312	0.00484	0.00022	0.25	98.5	6.4	97.7	4.4	96.9	1.6	98%
LBL-113-12	40.5	2415	0.33	0.01461	0.00023	0.09632	0.00635	0.04757	0.00306	0.00512	0.00023	0.24	93.4	5.9	103.3	4.6	93.5	1.5	99%
LBL-113-13	30.8	1632	0.59	0.01553	0.00043	0.10352	0.00742	0.04889	0.00325	0.00592	0.00032	0.39	100.0	6.8	119.2	6.4	99.3	2.7	99%
LBL-113-14	22.7	1322	0.32	0.01519	0.00040	0.09136	0.00636	0.04384	0.00304	0.00540	0.00035	0.37	88.8	5.9	108.8	7.0	97.2	2.5	90%
LBL-113-15	14.5	754	0.51	0.01548	0.00038	0.10164	0.00818	0.04784	0.00373	0.00561	0.00026	0.30	98.3	7.5	113.1	5.2	99.0	2.4	99%

(*continued on next page*)

Table 3 (*continued*)

Analysis	Pb	U	Th/U	Atomic Ratios								rho	Ages(Ma)						Concordance
	(ppm)			$^{206}Pb/^{238}U$	± 1σ	$^{207}Pb/^{235}U$	± 1σ	$^{207}Pb/^{206}Pb$	± 1σ	$^{208}Pb/^{232}Th$	± 1σ		$^{207}Pb/^{235}U$	± 1σ	$^{208}Pb/^{232}Th$	± 1σ	$^{206}Pb/^{238}U$	± 1σ	
LBL-113-16	15.8	815	0.82	0.01545	0.00039	0.11032	0.00970	0.05174	0.00428	0.00525	0.00036	0.29	106.3	8.9	105.7	7.3	98.8	2.5	92%
LBL-113-17	13.0	561	0.32	0.02040	0.00052	0.12608	0.01066	0.04470	0.00367	0.00539	0.00042	0.30	120.6	9.6	108.7	8.5	130.2	3.3	92%
LBL-113-18	24.7	1457	0.20	0.01525	0.00035	0.10151	0.00710	0.04765	0.00308	0.00515	0.00027	0.33	98.2	6.5	103.7	5.4	97.6	2.2	99%
LBL-113-19	22.7	1503	0.24	0.01306	0.00027	0.09074	0.00636	0.04982	0.00334	0.00558	0.00029	0.29	88.2	5.9	112.5	5.8	83.7	1.7	94%
LBL-113-20	17.8	936	0.60	0.01547	0.00036	0.10486	0.00868	0.04877	0.00410	0.00488	0.00027	0.28	101.3	8.0	98.4	5.5	99.0	2.3	97%
LBL-113-21	33.4	2203	0.30	0.01378	0.00034	0.09448	0.00876	0.04861	0.00429	0.00473	0.00030	0.26	91.7	8.1	95.4	6.1	88.2	2.1	96%
LBL-113-22	43.3	2605	0.25	0.01497	0.00025	0.09486	0.00666	0.04546	0.00325	0.00515	0.00030	0.23	92.0	6.2	103.8	6.0	95.8	1.6	95%
LBL-113-23	20.5	1184	0.39	0.01528	0.00039	0.11099	0.01033	0.05170	0.00444	0.00530	0.00031	0.28	106.9	9.4	106.8	6.2	97.8	2.5	91%
LBL-113-24	20.3	1192	0.27	0.01543	0.00037	0.10960	0.01091	0.05059	0.00468	0.00537	0.00029	0.24	105.6	10.0	108.2	5.7	98.7	2.3	93%
LBL-113-25	15.0	795	0.49	0.01587	0.00031	0.11607	0.01126	0.05262	0.00499	0.00487	0.00025	0.20	111.5	10.2	98.2	4.9	101.5	2.0	90%

Muscovite is a common mineral within the root zone of porphyry Cu deposits (Seedorff et al., 2008) and in epithermal deposits, as exemplified by the Cerro de Pasco deposit in Peru (Baumgartner et al., 2008), the Comstock deposit in Nevada (Hudson, 2003), the Rosario deposit in Chile (Masterman et al., 2005), and the Peak Hill deposit in Australia (Squire et al., 2007). Muscovite has a radiogenic argon closure temperatures of either 270 °C–325 °C (Snee et al., 1988) or up to 410 °C (Hames and Bowring, 1994; Kirschner et al., 1996). This means that muscovite ^{40}Ar-^{39}Ar results should more accurately record the mineralization age of an ore deposit that underwent multi-stage hydrothermal activity.

Some quartz-muscovite-pyrite veins (Fig. 5A) cut the alunite-dickite alteration within the ZOF (Fig. 5B), indicating that the muscovite formed later than the alteration (Fig. 5A and C). This indicates that the ^{40}Ar-^{39}Ar plateau age (110.4 ± 1.3 Ma) of the muscovite represents a minimum age for the alunite-dickite alteration. This in turn indicates that the hydrothermal activity associated with the formation of the HSE Cu-Au mineralization occurred before ca. 110 Ma.

The Q-Alu-Di-Phy zone also contains disseminated muscovite and quartz-muscovite-dickite-pyrite veinlets in volcanic breccia (Fig. 4A). The planar crystal boundaries between muscovite and dickite (Fig. 4B) suggest that these minerals formed contemporaneously. On a smaller scale, the quartz-muscovite-dickite-pyrite assemblage is cut by an alunite-altered breccia (Fig. 4C, 4D). These observations suggest that the epithermal mineralization-related muscovite formed contemporaneously with the dickite-alteration but earlier than the alunite-alteration. The ^{40}Ar-^{39}Ar plateau age (113.4 ± 1.1 Ma) of the muscovite therefore constrains the upper age of the alunite alteration to ca.113 Ma. In addition, the crypto-explosive breccia, which contains clasts of hydrothermal sulfide mineralization (Fig. 3E), yields a zircon U-Pb age of 112.9 ± 1.2 Ma, representing a minimum age for the hydrothermal sulfide ores within the deposit (Fig. 3E). The ^{40}Ar-^{39}Ar plateau age of the muscovite that is cogenetic with the dickite is within uncertainty of the zircon U-Pb age of the crypto-explosive breccia, again suggesting that the HSE Cu-Au mineralization formed at ca. 113 Ma.

The new zircon U-Pb age of 103.8 ± 0.9 Ma for the Luoboling granodiorite porphyry associated with the Cu-Mo mineralization is consistent with previously reported molybdenite Re-Os isochron ages of 104.9 ± 1.6 (Liang et al., 2012) and 104.6 ± 1.0 Ma (Zhong et al., 2014) for the deposit. These age data indicate that the porphyry Cu-Mo mineralization formed ca. 9 Myr later than the main HSE mineralization. In other words, the adjacent HSE Au-Cu and porphyry Cu-Mo deposits within the ZOF are associated with two distinct episodes of magmatism and are not genetically linked. This view is further supported by recent fluid mapping (Zhong et al., 2018) and isotopic research (Li and Jiang, 2017) in the ZOF, both of which indicate that the Luoboling porphyry was not the heat source that drove the formation of the Zijinshan HSE deposit (Zhong et al., 2018) and that the two deposits have different sources (Li and Jiang, 2017).

5.3. Magmatic sources evolution and implications for metal associations

The various metal associations within the Zijinshan Cu-Au and Luoboling Cu-Mo deposits were originally thought to reflect metal zoning resulting from hydrothermal precipitation in a porphyry-epithermal system (e.g., Li and Jiang, 2017). However, our new geochronological data indicate that these two deposits formed during distinct hydrothermal events. The fact that these two adjacent deposits are not genetically linked means that their contrasting metal associations reflect different magmatic processes.

Magmatic-hydrothermal deposits have variable metal associations and Cu/Au ratios (Candela, 1992; Halter et al., 2002; Singer et al., 2005; Richards, 2011) that are controlled by the nature of the sources of magmas associated with the deposits. For example, the mantle contains higher concentrations of Cu (145 ppm; Gill, 1981) and Au (Taylor

Table 4
Hf isotopic compositions of representative igneous samples from the Zijinshan orefield.

Spot	Age/(Ma)	$^{176}Yb/^{177}Hf$	δ	$^{176}Lu/^{177}Hf$	δ	$^{176}Hf/^{177}Hf$	δ	$\varepsilon_{Hf}(0)$	$\varepsilon_{Hf}(t)$	T_{DM2}/(Ma)
Crypto-explosive breccias										
ZJ1505-05	113.4	0.083882	0.000994	0.002035	0.000020	0.282686	0.000014	−3.1	−0.7	1215
ZJ1505-04	113.4	0.062338	0.000284	0.001475	0.000005	0.282665	0.000013	−3.8	−1.4	1258
ZJ1505-09	113.4	0.056803	0.000200	0.001370	0.000001	0.282718	0.000013	−1.9	0.5	1140
ZJ1505-15	113.4	0.065723	0.000326	0.001575	0.000005	0.282676	0.000014	−3.4	−1.0	1235
ZJ1505-20	113.4	0.060213	0.000106	0.001401	0.000002	0.282661	0.000014	−3.9	−1.5	1268
ZJ1505-21	113.4	0.058024	0.000133	0.001414	0.000001	0.282712	0.000016	−2.1	0.3	1153
ZJ1505-28	113.4	0.060304	0.000363	0.001442	0.000007	0.282671	0.000014	−3.6	−1.2	1246
Luoboling granodiorite porphyry										
LBL-82-1	103.5	0.026937	0.000171	0.001213	0.000006	0.282608	0.000008	−5.8	−3.6	1391
LBL-82-2	103.5	0.010390	0.000115	0.000475	0.000004	0.282674	0.000010	−3.5	−1.2	1241
LBL-82-3	103.5	0.019110	0.000213	0.000876	0.000011	0.282661	0.000009	−3.9	−1.7	1271
LBL-82-4	103.5	0.019799	0.000163	0.000905	0.000004	0.282634	0.000009	−4.9	−2.7	1332
LBL-82-5	103.5	0.017867	0.000052	0.000795	0.000002	0.282624	0.000009	−5.2	−3.0	1354
LBL-82-7	103.5	0.022746	0.000166	0.000991	0.000010	0.282613	0.000010	−5.6	−3.4	1380
LBL-82-8	103.5	0.018711	0.000122	0.000861	0.000004	0.282676	0.000009	−3.4	−1.2	1238
LBL-82-9	103.5	0.019872	0.000070	0.000907	0.000002	0.282594	0.000008	−6.3	−4.1	1423
LBL-82-10	103.5	0.025264	0.000256	0.001103	0.000005	0.282583	0.000010	−6.7	−4.5	1447
LBL-82-11	103.5	0.017775	0.000204	0.000795	0.000006	0.282673	0.000010	−3.5	−1.3	1245
LBL-82-12	103.5	0.021910	0.000062	0.000967	0.000002	0.282638	0.000008	−4.7	−2.6	1324
LBL-82-13	103.5	0.020799	0.000223	0.000912	0.000007	0.282640	0.000008	−4.7	−2.5	1320
LBL-82-14	103.5	0.020703	0.000234	0.000934	0.000009	0.282654	0.000008	−4.2	−2.0	1288
LBL-82-15	103.5	0.017999	0.000154	0.000755	0.000006	0.282668	0.000009	−3.7	−1.5	1255
LBL-82-16	103.5	0.018654	0.000410	0.000817	0.000019	0.282628	0.000009	−5.1	−2.9	1345
LBL-82-17	103.5	0.019384	0.000208	0.000868	0.000007	0.282671	0.000008	−3.6	−1.4	1250
LBL-82-19	103.5	0.018422	0.000120	0.000849	0.000006	0.282615	0.000009	−5.5	−3.3	1374
Barren Luoboling granodiorite										
LBL-113-6	98.5	0.033544	0.000146	0.001458	0.000004	0.282542	0.000008	−8.1	−6.1	1545
LBL-113-7	98.5	0.035207	0.000059	0.001534	0.000004	0.282592	0.000009	−6.4	−4.3	1432
LBL-113-9	98.5	0.040635	0.000176	0.001757	0.000013	0.282486	0.000010	−10.1	−8.1	1670
LBL-113-11	98.5	0.048326	0.000399	0.002137	0.000021	0.282531	0.000008	−8.5	−6.5	1570
LBL-113-12	98.5	0.042573	0.000525	0.001824	0.000022	0.282585	0.000009	−6.6	−4.6	1449
LBL-113-13	98.5	0.032684	0.000646	0.001365	0.000021	0.282536	0.000011	−8.3	−6.3	1556
LBL-113-14	98.5	0.023895	0.000661	0.001027	0.000029	0.282531	0.000008	−8.5	−6.4	1566
LBL-113-15	98.5	0.048589	0.000801	0.001856	0.000022	0.282484	0.000009	−10.2	−8.1	1675
LBL-113-16	98.5	0.034157	0.000615	0.001309	0.000023	0.282340	0.000009	−15.3	−13.2	1994
LBL-113-18	98.5	0.027732	0.000385	0.001166	0.000012	0.282513	0.000010	−9.2	−7.1	1608
LBL-113-20	98.5	0.033418	0.000225	0.001412	0.000008	0.282498	0.000009	−9.7	−7.6	1642
LBL-113-22	98.5	0.062472	0.001512	0.002665	0.000063	0.282564	0.000010	−7.4	−5.4	1500
LBL-113-23	98.5	0.033487	0.000371	0.001483	0.000011	0.282462	0.000010	−10.9	−8.9	1722

and McLennan, 1985; Rudnick and Gao, 2003) than the bulk continental crust (Cu = 27 ppm; Rudnick and Gao, 2003), whereas the majority of Mo is derived from continental crustal sources (White et al., 1981; Farmer and DePaolo, 1984; Klemm et al., 2008). This means that magmas derived from different sources are usually associated with mineral deposits with different metal compositions (e.g., Richards, 2011). In addition, magmatic processes might also affect the metal associations and metal ratios within mineral deposits (e.g., Halter et al., 2002; Richards, 2009; Huang et al., 2017a, 2017b). Residual sulfide phases in sources or magma could affect the Cu/Au ratios of porphyry deposits because the partition coefficients for Au partitioning into sulfide phases relative to silicate melts ($D_{(Au)}^{sulfide/silicate\ melt}$ = 2000–20,000, Li and Audétat, 2013) are larger than those for both Cu ($D_{(Cu)}^{sulfide/silicate\ melt}$ = 550–10,000; Lynton et al., 1993; Gaetani and Grove, 1997; Jugo et al., 1999; Halter et al., 2002)and Mo ($D_{(Mo)}^{sulfide/silicate\ melt}$ = 15–200, Li and Audétat, 2012). However, the Cretaceous magmatism recorded within the ZOF is highly oxidized (Duan et al., 2017; Li and Jiang, 2017; Xu et al., 2017), which could have suppressed the fractionation of sulfide during the evolution of magmas within this system. Consequently, the different metal associations within the Zijinshan and Luoboling deposits were possibly controlled by variations in magma source composition rather than the effect of residual sulfide phases.

The crypto-breccia formed at a similar time (112.9 ± 1.2 Ma) to the epithermal Au-Cu mineralization (113.4 ± 1.1 Ma) in the study area and contains ore-clasts of ore material within a mineralized matrix (Fig. 3E and F). This suggests that the crypto-breccia formed from the magma that generated the Zijinshan HSE deposit. The zircon ε_{Hf} (t) values of the ZOF igneous rocks show a positive correlation with their zircon U-Pb ages (Fig. 11), where crypto-explosive breccia associated with the Zijinshan HSE Au-Cu mineralization (112.9 ± 1.2 Ma), the Luoboling granodiorite porphyry (103.8 ± 0.9 Ma), and the barren Luoboling granodiorite (98.1 ± 1.1 Ma) have ε_{Hf} (t) values of −1.5 to −0.5, −4.5 to −1.2, and −13.2 to −4.3, respectively (Table 4). In addition, other Cretaceous igneous rocks within the ZOF, including the Sifang granodiorite (Liang et al., 2013; Li and Jiang, 2014a; Duan et al., 2017) and volcanic rocks in this area (Liang et al., 2013), yield zircon ε_{Hf} (t) values that positively correlated with their U-Pb ages (Fig. 11). These latter correlations indicate that the ZOF records the long-live Cretaceous mixing between mantle- and crustal-derived materials, where crustal material was progressively added to mantle-derived magmas (Fig. 12). The ca. 103 Ma magmas associated with the porphyry Cu-Mo mineralization were most likely derived from a source containing more crustal material (Fig. 12B) than the ca. 110 Ma magmas associated with the epithermal Au-Cu mineralization in the ZOF (Fig. 12A). These distinct source variations could be a controlling factor on the different metal associations present within the adjacent HSE Au-Cu and porphyry Cu-Mo deposits in the ZOF.

5.4. Implications for mineral exploration and future research

The present results indicate that the adjacent HSE Au-Cu and

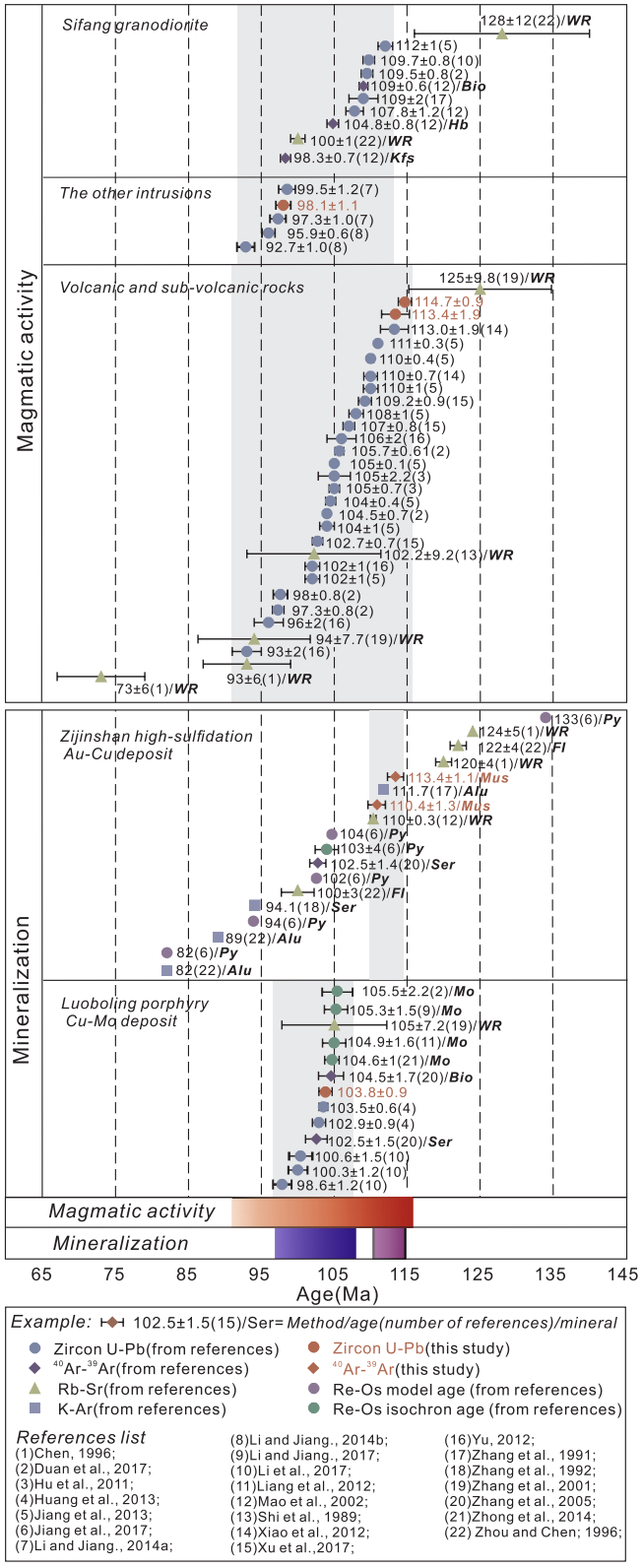

Fig. 10. Summary of published geochronological data from the ZOF. Abbreviations are as follows: Adu = adularia, Alu = alunite, Bio = biotite, FI = fluid inclusion, Hb = hornblende, Kfs = K-feldspar, Mo = molybdenite, Mus = muscovite, Py = pyrite, Ser = sericite, WR = whole rock.

porphyry Cu-Mo deposits in the ZOF did not form from the same hydrothermal system and that the porphyry Cu-Mo deposit do not represent the 'root' of the HSE Au-Cu deposit. The generally close spatial

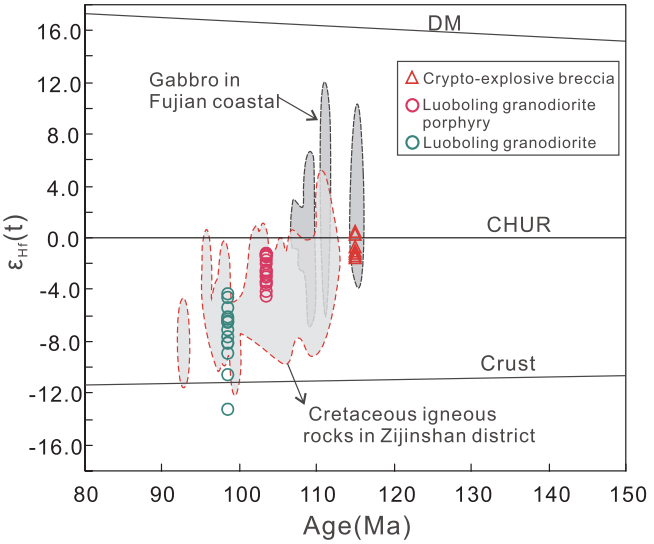

Fig. 11. Zircon ε_{Hf} (t) versus U-Pb age diagram for the crypto-explosive breccia, Luoboling granodiorite, and the barren Luoboling granodiorite. Data for Cretaceous igneous rocks in the Zijinshan area are from Liang et al. (2013), Li et al. (2014), and Li and Jiang (2014a,b), and data for Cretaceous gabbros in the Fujian coastal area are from Li et al. (2014). Abbreviations are as follows: DM = depleted mantle; CHUR = chondritic uniform reservoir.

and genetic associations between HSE Au-Cu and porphyry Au-Cu deposits reported elsewhere (Sillitoe, 1989; Hedenquist and Lowenstern, 1994; Arribas et al., 1995; Sillitoe, 1997), combined with the well-preserved epithermal deposits within the ZOF, suggest that deeper parts of the ZOF contain porphyry Au-Cu mineralization that is genetically related to the HSE Au-Cu mineralization (Fig. 12A). This indicates that the deeper parts of the ZOF warrant future exploration for porphyry Au-Cu mineralization.

Despite previous research that suggests that adjacent porphyry and HSE deposits tend to be cogenetic and contemporaneous (e.g., Arribas et al., 1995; Muntean and Einaudi, 2001; Table 1), this study demonstrates that not all adjacent porphyry and HSE deposits, especially those with different metal associations, are cogenetic. Precise geochronological and isotopic analysis help to advance our understanding of the relationships between these different mineral deposit types and provide vital information for future exploration.

6. Conclusions

The main conclusions of this study can be summarized as follows.

(1) The ^{40}Ar-^{39}Ar age (113.4 ± 1.1 Ma) of muscovite that was cogenetic with dickite and the zircon U-Pb age of a hydrothermal ore-bearing volcanic breccia (112. 9 ± 1.2 Ma) suggest that the main HSE mineralization event occurred at ca. 113 Ma. In addition, the ^{40}Ar-^{39}Ar age (110.4 ± 1.3 Ma) of muscovite from a quartz-muscovite-pyrite vein that cuts the alunite-dickite alteration suggests that the alunite-dickite alteration related to the Zijinshan HSE Au-Cu deposit formed before ca. 110 Ma. The adjacent Luoboling porphyry Cu-Mo deposit yielded a zircon U-Pb age of 103.8 ± 0.9 Ma. These adjacent epithermal and porphyry deposits most likely formed during two distinct episodes of magmatism within the ZOF.

(2) Zircon Lu-Hf isotopic compositions indicate that the magma associated with the porphyry Cu-Mo mineralization was derived from a source containing more crustal material than the volcanic rocks associated with the HSE Au-Cu mineralization. These distinct sources can account for the different metal associations of the adjacent HSE Au-Cu and porphyry Cu-Mo deposits within the ZOF.

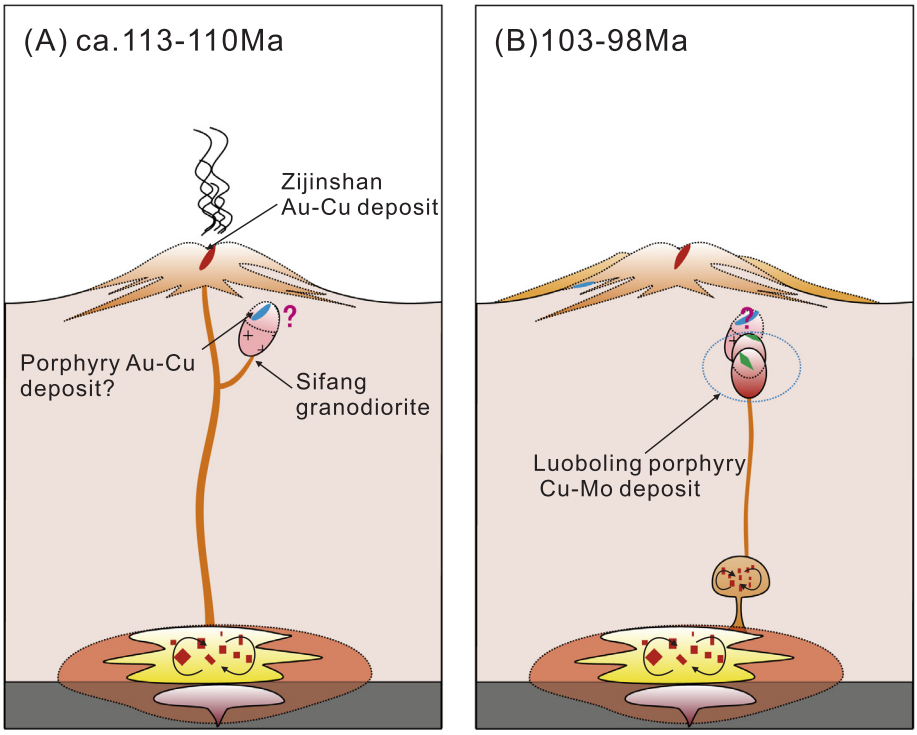

Fig. 12. Schematic diagrams showing a possible model for the genesis of Cretaceous igneous rocks and related mineralization within the ZOF. (A) Mantle-derived magmas mixed with crustal material to produce Au-Cu enriched magmas that were emplaced in the ZOF at ca. 113 Ma, forming the Zijinshan HSE Au-Cu deposit. (B) Continuing crust-mantle mixing added crustal materials into the magmas in this area, eventually generating the Cu-Mo enriched magmas that were emplaced at ca. 103 Ma and formed the Luoboling porphyry Cu-Mo deposit.

(3) Not all adjacent porphyry and HSE deposits are cogenetic. In addition, the deeper part of the Zijinshan HSE Au-Cu deposit could represent a favorable target for porphyry Au-Cu exploration within the ZOF.

Acknowledgement

We thank Zijin Mining Group Co, Ltd for assistance during our field work. This work was financially supported by the Natural Science Foundation of China (Grants 41502073 and 41772065) and the National Key R&D Program of China (Grant 2016YFC0600407). I thank Dr. Plotinskaya and two anonymous reviewers for their constructive comments and suggestions. This is contribution No. IS-2587 from GIGCAS.

References

Arribas, A., Hedenquist, J.W., Itaya, T., Okada, T., Concepcion, R.A., Garcia, J.S., 1995. Contemporaneous formation of adjacent porphyry and epithermal Cu-Au deposits over 300 Ka in Northern Luzon, Philippines. Geology 23, 337–340.

Baumgartner, R., Fontbote, L., Vennemann, T., 2008. Mineral zoning and geochemistry of epithermal polymetallic Zn-Pb-Ag-Cu-Bi mineralization at Cerro de Pasco, Peru. Econ. Geol. 103, 493–537.

Bissig, T., Cooke, D.R., 2014. Introduction to the special issue devoted to alkalic porphyry Cu-Au and epithermal Au deposits. Econ. Geol. 109, 819–825.

Black, L.P., Kamo, S.L., Allen, C.M., Aleinikoff, J.N., Davis, D.W., Korsch, R.J., Foudoulis, C., 2003. TEMORA 1: a new zircon standard for Phanerozoic U-Pb geochronology. Chem. Geol. 200, 155–170.

Candela, P.A., 1992. Controls on ore metal ratios in granite-related ore systems: an experimental and computational approach. Trans. R. Soc. Edinburgh Earth Sci. 83 (1–2), 317–326.

Cardon, O., Reisberg, L., Andre-Mayer, A.S., Leroy, J., Milu, V., Zimmermann, C., 2008. Re-Os systematics of pyrite from the bolcana porphyry copper deposit, apuseni mountains, romania. Econ. Geol. 103 (8), 1695–1702.

Chang, Z.S., Hedenquist, J.W., White, N.C., Cooke, D.R., Roach, M., Deyell, C.L., Garcia, J., Gemmell, J.B., McKnight, S., Cuison, A.L., 2011. Exploration tools for linked porphyry and epithermal deposits: example from the mankayan intrusion-centered Cu-Au District, Luzon, Philippines. Econ. Geol. 106, 1365–1398.

Chen, H.S., 1996. The research on the mineralization chronology and isotopic exploration assessment for Zijinshan copper-gold deposit. Geotectonica et Metallogenia v. 20, 343–350.

Chen, C.H., Lee, C.Y., Shinjo, R., 2008. Was there Jurassic paleo-Pacific subduction in South China?: constraints from 40Ar-39Ar dating, element and Sr-Nd-Pb isotopic geochemistry of the Mesozoic basalts. Lithos 106, 83–92.

Chen, J., Chen, Y.J., Zhong, J., Sun, Y., Qi, J.P., Li, J., 2015. Geological and ore-fluid characteristics of Longjiangting Cu deposit in Zijinshan Orefield, Fujian Province, and their genetic implications. Mineral Deposits 34 (1), 98–118.

Cliff, R.A., Rickard, D., 1992. Isotope systematics of the Kiruna magnetite ores, Sweden. 2. evidence for a secondary event 400 My after ore formation. Econ. Geol. Bull. Soc. Econ. Geol. 87, 1121–1129.

Cooke, D.R., Deyell, C.L., Waters, P.J., Gonzales, R.I., Zaw, K., 2011. Evidence for magmatic-hydrothermal fluids and ore-forming processes in epithermal and porphyry deposits of the Baguio District, Philippines. Econ. Geol. 106, 1399–1424.

Deyell, C., Hedenquist, J., 2011. Trace element geochemistry of enargite in the Mankayan district, Philippines. Econ. Geol. 106, 1465–1478.

Duan, G., Chen, H., Hollings, P., Qi, J., Xu, C., Zhang, S., Xiao, B., Liu, G., Liu, J., 2017. The Mesozoic magmatic sources and tectonic setting of the Zijinshan mineral field, South China: constraints from geochronology and geochemistry of igneous rocks in the Southeastern Ore Segment. Ore Geol. Rev. 80, 800–827.

Farmer, G.L., DePaolo, D.J., 1984. Origin of Mesozoic and Tertiary granite in the western United States and implications for pre-Mesozoic crustal structure, 2. Nd and Sr isotopic studies of unmineralized and Cu- and Mo-mineralized granite in the Precambrian craton. J. Geophys. Res. 89, 10141–10160.

Franchini, M., Impiccini, A., Lentz, D., Rios, J., O'Leary, S., Pons, J., Schalamuk, A., 2011. Porphyry to epithermal transition in the Agua Rica polymetallic deposit, Catamarca, Argentina: an integrated petrologic analysis of ore and alteration parageneses. Ore Geol. Rev. 41, 49–74.

Gaetani, G.A., Grove, L.T., 1997. Partitioning of moderately siderophile elements among olivine, silicate melt, and sulfide melt: constraints on core formation in the earth and mars. Geochim. Cosmochim. Acta 61, 1829–1841.

Gammons, C.H., WilliamsJones, A.E., 1997. Chemical mobility of gold in the porphyry-epithermal environment. Econ. Geol. 92, 45–59.

Gill, J.B., 1981. In: Orogenic Andesites and Plate Tectonics. Springer-Verlag, New York, pp. 390.

Grabezhev, A.I., Bea, F., Montero, M.P., Fershtater, G.B., 2013. The U-Pb SHRIMP age of zircons from diorites of the Tomino-Bereznyaki ore field (South Urals, Russia): evolution of porphyry Cu epithermal Au-Ag system. Russ. Geol. Geophys 54, 1332–1339.

Halter, W.E., Pettke, T., Heinrich, C.A., 2002. The origin of Cu/Au ratios in porphyry-type ore deposits. Science 296, 1844–1846.

Hames, W.E., Bowring, S.A., 1994. An Empirical-evaluation of the argon diffusion geometry in muscovite. Earth Planet. Sci. Lett. 124, 161–167.

Harrison, T.M., Mcdougall, I., 1982. The thermal significance of potassium-feldspar K-Ar ages inferred from Ar^{40}/Ar^{39} age spectrum results. Geochim. Cosmochim. Acta 46, 1811–1820.

Hedenquist, J.W., Lowenstern, J.B., 1994. The Role of magmas in the formation of hydrothermal ore-deposits. Nature 370, 519–527.

Hedenquist, J.W., Arribas, A., Reynolds, T.J., 1998. Evolution of an intrusion-centered hydrothermal system: far Southeast-Lepanto porphyry and epithermal Cu-Au deposits, Philippines. Econ. Geol. 93, 373–404.

Hedenquist, J.W., Taran, Y.A., 2013. Modeling the formation of advanced argillic lithocaps: volcanic vapor condensation above porphyry intrusions. Econ. Geol. 108, 1523–1540.

Heinrich, C.A., 2003. Magmatic vapour condensation and the relation between

porphyries and epithermal Au-(Cu-As) mineralisation: thermodynamic constraints. Mineral Explor. Sustainable Dev. 1 and 2, 279–282.
Heinrich, C.A., Gunther, D., Audetat, A., Ulrich, T., Frischknecht, R., 1999. Metal fractionation between magmatic brine and vapor, determined by microanalysis of fluid inclusions. Geology 27, 755–758.
Heinrich, C.A., Driesner, T., Stefansson, A., Seward, T.M., 2004. Magmatic vapor contraction and the transport of gold from the porphyry environment to epithermal ore deposits. Geology 32, 761–764.
Hemley, J.J., Hunt, J.P., 1992. Hydrothermal ore-forming processes in the light of studies in rock-buffered systems.2. some general geologic applicationsg. Econ. Geol. 87, 23–43.
Hoskin, P.W.O., Schaltegger, U., 2003. The composition of zircon and igneous and metamorphic petrogenesis. Zircon 53, 27–62.
Hu, C.J., Huang, W.T., Bao, Z.W., Liang, H.Y., Wang, C.L., 2012. LA-ICP-MS zirocn U-Pb dating of the dacite porphyry from Zijinshan Cu-Au deposit and its metallogenetic implications. Geotectonica et Metallogenia 36, 284–295.
Huang, R.S., 2008. Igneous series and epithermal porphyry Cu-Au-Ag mineralization system in the Zijinshan ore field, Fujian Province. J. Geomech. 14, 74–86.
Huang, W.T., Li, J., Liang, H.Y., Wang, C.L., Lin, S.P., Wang, X.Z., 2013. Zircon LA-ICP-MS U-Pb ages and highly oxidized features of magma associated with Luoboling porphyry Cu-Mo deposit in Zijinshan ore field, Fujian Province. Acta Petrol. Sin. 29 (1), 283–293.
Huang, W.T., Liang, H.Y., Wu, J., Zou, Y.Q., Zhang, J., 2017a. Formation of porphyry Mo deposit in a deep fault zone, example from the Dabaoshan porphyry Mo deposit in northern Guangdong, South China. Ore Geol. Rev. 81, 940–952.
Huang, W.T., Wu, J., Zhang, J., Liang, H.Y., Qiu, X.L., 2017b. Geochemistry and Hf-Nd isotope characteristics and forming processes of the Yuntoujie granites associated with W-Mo deposit, Guangxi, South China. Ore Geol. Rev. 81, 953–964.
Hudson, D.M., 2003. Epithermal alteration and mineralization in the Comstock district, Nevada. Econ. Geol. 98, 367–385.
Jiang, S.H., Liang, Q.L., Bagas, L., Wang, S.H., Nie, F.J., Liu, Y.F., 2013. Geodynamic setting of the Zijinshan porphyry-epithermal Cu-Au-Mo-Ag ore system, SW Fujian Province, China: constrains from the geochronology and geochemistry of the igneous rocks. Ore Geol. Rev. 53, 287–305.
Jiang, S.H., Bagas, L., Liang, Q.L., 2017. Pyrite Re-Os isotope systematics at the Zijinshan deposit of SW Fujian, China: constraints on the timing and source of Cu-Au mineralization. Ore Geol. Rev. 80, 612–622.
Jochum, K.P., Weis, U., Stoll, B., Kuzmin, D., Yang, Q.C., Raczek, I., Jacob, D.E., Stracke, A., Birbaum, K., Frick, D.A., Gunther, D., Enzweiler, J., 2011. Determination of reference values for NIST SRM 610–617 glasses following ISO guidelines. Geostand. Geoanal. Res. 35, 397–429.
John, D.A., Ayuso, R.A., Barton, M.D., Blakely, R.J., Bodnar, R.J., Dilles, J.H., Gray, F., Graybeal, F.T., Mars, J.C., McPhee, D.K., Seal, R.R., Taylor, R.D., Vikre, P.G., 2010. Porphyry copper deposit model, chap. B of Mineral deposit models for resource assessment. 2010-5070-B. U.S. Geological Survey Scientific Investigations Report, pp. 169.
Jugo, P.J., Candela, P.A., Peccoli, P.M., 1999. Magmatic sulfides and Au: Cu ratios in porphyry deposits: an experimental study of copper and gold partitioning at 850°C, 100MPa in a haplogranitic melt-pyrrhotite-intermediate solid solution-gold metal assemblage, at gas saturation. Lithos v. 46, 573–589.
Kirschner, D.L., Cosca, M.A., Masson, H., Hunziker, J.C., 1996. Staircase Ar^{40}/Ar^{39} spectra of fine-grained-white mica: timing and duration of deformation and empirical constraints on argon diffusion. Geology v. 24, 747–750.
Klemm, L.M., Pettke, T., Heinrich, C.A., 2008. Fluid and source magma evolution of the Questa porphyry Mo deposit, New Mexico, USA. Mineral. Deposita 43, 533–552.
Koppers, A.A., 2002. ArArCALC-software for $^{40}Ar/^{39}Ar$ age calculations. Comput. Geosci. 28, 605–619.
Li, Y., Audétat, A., 2013. Gold solubility and partitioning between sulfide liquid, monosulfide solid solution and hydrous mantle melts: Implications for the formation of Au-rich magmas and crust–mantle differentiation. Geochimica Et Cosmochimica Acta 118 (10), 247–262.
Li, Y., Audétat, A., 2012. Partitioning of V, Mn Co, Ni, Cu, Zn, As, Mo, Ag, Sn, Sb, W, Au, Pb, and Bi between sulfide phases and hydrous basanite melt at upper mantle conditions. Earth Planet. Sci. Lett. 355–356, 327–340.
Li, Z., Qiu, J.S., Yang, X.M., 2014. A review of the geochronology and geochemistry of Late Yanshanian (Cretaceous) plutons along the Fujian coastal area of southeastern China: implications for magma evolution related to slab break-off and rollback in the Cretaceous. Earth Sci. Rev. 128, 232–248.
Li, C.Y., Hao, X.L., Liu, J.Q., Ling, M.X., Ding, X., Zhang, H., Sun, W.D., 2017. The formation of Luoboling porphyry Cu-Mo deposit: constraints from zircon and apatite. Lithos 272–273, 291–300.
Li, Y., Selby, D., Li, X.H., Ottley, C.J., 2018. Multisourced metals enriched by magmatic-hydrothermal fluid in stratabound deposits of the middle-lower yangtze river metallogenic belt, China. Geology 46 (5), 391–394.
Li, B., Jiang, S.Y., 2014a. Geochronology and geochemistry of Cretaceous Nanshanping alkaline rocks from the Zijinshan district in Fujian Province, South China: implications for crust-mantle interaction and lithospheric extension. J. Asian Earth Sci. 93, 253–274.
Li, B., Jiang, S.Y., 2014b. A subduction-related metasomatically enriched mantle origin for the Luoboling and Zhongliao Cretaceous granitoids from South China: implications for magma evolution and Cu-Mo mineralization. Int. Geol. Rev. 57, 1239–1266.
Li, B., Jiang, S.Y., 2017. Genesis of the giant Zijinshan epithermal Cu-Au and Luoboling porphyry deposits in the Zijinshan ore district, Fujian Province, SE China: a multi-isotope and trace element inverstigation. Ore Geol. Rev. 88, 753–767.
Li, X.H., Long, W.G., Li, Q.L., Liu, Y., Zheng, Y.F., Yang, Y.H., Chamberlain, K.R., Wan, D.F., Guo, C.H., Wang, X.C., Tao, H., 2010. Penglai Zircon Megacrysts: a potential new working reference material for microbeam determination of Hf-O isotopes and U-Pb age. Geostand. Geoanal. Res. 34, 117–134.
Li, B., Zhao, K.D., Yang, S.Y., Dai, B.Z., 2013. Petrogenesis of the porphyritic dacite from Ermiaogou Cu-Au deposit in Zijinshan ore field and its metallogenetic implications. Acta Petrol. Sin. 29 (12), 4167–4185.
Liang, H.Y., Campbell, I.H., Allen, C., Sun, W.D., Liu, C.Q., Yu, H.X., Xie, Y.W., Zhang, Y.Q., 2006. Zircon Ce^{4+}/Ce^{3+} ratios and ages for Yulong ore-bearing porphyries in eastern Tibet. Miner. Deposita 41, 152–159.
Liang, Q.L., Jiang, S.H., Wang, S.H., Li, C., Zeng, F.G., 2012. Re-Os Dating of Molybdenite from the Luoboling Porphyry Cu-Mo Deposit in the Zijinshan Ore Field of Fujian Province and Its Geological Significance. Acta Geol. Sin. 86, 1113–1118.
Liang, Q.L., Jiang, S.H., Wang, S.H., Liu, Y.F., Bai, D.M., Chen, C.L., 2013. Petrogenesis of Mesozoic magmatic rocks in Zijinshan area: constraints from zircon Hf isotope evidence. Acta Petrologica et Mineralogica 32, 318–328.
Liu, Y., Hu, Z., Zong, K., Gao, C., Gao, S., Xu, J., Chen, H., 2010. Reappraisement and refinement of zircon U-Pb isotope and trace element analyses by LA-ICP-MS. Chin. Sci. Bull. 55, 1535–1546.
Longo, A.A., Dilles, J.H., Grunder, A.L., Duncan, R., 2010. Evolution of calc-alkaline volcanism and associated hydrothermal gold deposits at Yanacocha, Peru. Econ. Geol. 105, 1191–1240.
Ludwig, K.R., 2003, User's manual for Isoplot 3.00: a geochronological toolkit for Microsoft Excel.
Lynton, S.J., Candela, P.A., Piccoli, P.M., 1993. An experimental study of the partitioning of copper between pyrrhotite and a high silica rhyolite melt. Econ. Geol. 88, 901–915.
Mao, J.R., Tao, K.Y., Lee, J.Y., Xie, F.G., Xu, N.Z., 2002. Geochronology and geochemical characteristics in late Mesozoic Sifang pluton, southwestern Fujian, and their significanc. Acta Petrol. Sin. 18 (4), 449–458.
Mao, J.R., Xu, N.Z., Hu, Q., Li, J.Y., Xie, G.F., 2004. Geochronology and geochemical characteristics in Mesozoic granodioriticrocks in southwestern Fujian, and their tectonic evolution. J. Jilin Univ. (Earth Sci. Ed.) 34, 12–19.
Masterman, G.J., Cooke, D.R., Berry, R.F., Walshe, J.L., Lee, A.W., Clark, A.H., 2005. Fluid chemistry, structural setting, and emplacement history of the Rosario Cu-Mo porphyry and Cu-Ag-Au epithermal veins, Collahuasi district, northern Chile. Econ. Geol. 100, 835–862.
Maydagan, L., Fanchini, M., Rusk, B., Lentz, D.R., McFarlane, C., Impiccini, A., Rios, F.J., Rey, R., 2015. Porphyry to epithermal transition in the Altar Cu-(Au-Mo) deposit, Argentina, studied by cathodoluminescence, LA-ICP-MS, and fluid inclusion analysis. Econ. Geol. 110, 889–923.
Muntean, J.L., Einaudi, M.T., 2001. Porphyry-epithermal transition: Maricunga belt, northern Chile. Econ. Geol. 96, 743–772.
Pearce, N.J.G., Perkins, W.T., Westgate, J.A., Gorton, M.P., Jackson, S.E., Neal, C.R., Chenery, S.P., 1997. A compilation of new and published major and trace element data for NIST SRM 610 and NIST SRM 612 glass reference materials. Geostand. Newslett. 21, 115–144.
Perelló, J., Rojas, N., Devaux, C., Fava, L., and Etchart, E. Harman P., 1998. Discovery of the Agua Rica Porphyry Cu-Mo-Au Deposit, Catamarca Province, Northwestern Argentina, Part II: Geology: Australian Mineral Foundation Symposium, Perth, Proceedings, pp. 117–132.
Piquer, J., Cooke, D.R., Chen, J., Zhang, L., 2017. Synextensional Emplacement of Porphyry Cu-Mo and Epithermal Mineralization: The Zijinshan District, Southeastern China. Econ. Geol. 112, 1055–1074.
Pudack, C., Halter, W.E., Heinrich, C.A., Pettke, T., 2009. Evolution of magmatic vapor to gold-rich epithermal liquid: the porphyry to epithermal transition at Nevados de Famatina, Northwest Argentina. Econ. Geol. 104, 449–477.
Qiu, H.N., Wijbrans, J.R., 2006. When did amphibolite-facies overprinting occur in Dabieshan? Geochim. Cosmochim. Acta 70, A512.
Renne, P.R., Cassata, W.S., Morgan, L.E., 2009. The isotopic composition of atmospheric argon and Ar^{40}/Ar^{39} geochronology: time for a change? Quat. Geochronol. 4, 288–298.
Richards, J.P., 2009. Postsubduction porphyry Cu–Au and epithermal Au deposits: products of remelting of subduction-modified lithosphere. Geology v. 37, 247–250.
Richards, J.P., 2011. Magmatic to hydrothermal metal fluxes in convergent and collided margins. Ore Geol. Rev. 40, 1–26.
Richards, J.P., Wilkinson, D., Ullrich, T., 2006. Geology of the Sari Gunay Epithermal Gold Deposit, Northwest Iran. Econ. Geol. 101 (8), 1455–1496.
Rudnick, R.L., Gao, S., 2003. Composition of the continental crust. In: Rudnick, R.L. (Ed.), Treatise on Geochemistry 3: The Crust. Elsevier, Amsterdam, pp. 1–64.
Sang, H.Q., Wang, F., He, H.Y., Wang, Y.L., Yang, L.K., Zhu, R.X., 2006. Intercalibration of ZBH-25 biotite reference material untilized for K-Ar and ^{40}Ar-^{39}Ar age determination. Acta Petrol. Sin. v. 22(12), 3059–3078.
Seedorff, E., Barton, M.D., Stavast, W.J.A., Maher, D.J., 2008. Root zones of porphyry systems: extending the porphyry model to depth. Econ. Geol., vol 103, 939–956.
Sillitoe, R.H., 1989. Gold deposits in the Western Pacific Island Arcs: the magmatic connection. Econ. Geol. v. 6, 274–291.
Sillitoe, R.H., 1997. Characteristics and controls of the largest porphyry copper-gold and epithermal gold deposits in the circum-Pacific region. Aust. J. Earth Sci. 44, 373–388.
Sillitoe, R.H., 2010. Porphyry copper systems. Econ. Geol. 105, 3–41.
Singer, D.A., Berger, V.I., Menzie, W.D., Berger, B.R., 2005. Porphyry copper deposit density. Econ. Geol. Bull. Soc. Econ. Geol. 100, 491–514.
Snee, L.W., Sutter, J.F., Kelly, W.C., 1988. Thermochronology of economic mineral-deposits – dating the stages of mineralization at Panasqueira, Portugal, by high-precision Ar^{40}/Ar^{39} age spectrum techniques on muscovite. Econ. Geol. 83, 335–354.
Snee, L.W., 2002, Argon thermochronology of mineral deposits; a review of analytical methods, formulations, and selected applications. In: 2194, U.S.G.S.B. (Ed.).
So, C.S., Zhang, D.Q., Yun, S.T., Li, D.X., 1998. Alteration-mineralization zoning and fluid

inclusions of the high sulfidation epithermal Cu-Au mineralization at Zijinshan, Fujian Province, China. Econ. Geol. 93, 961–980.
Squire, R.J., Herrmann, W., Pape, D., Chalmers, D.I., 2007. Evolution of the peak hill high-sulfidation epithermal Au-Cu deposit, eastern Australia. Miner. Deposita 42, 489–503.
Taylor, S.R., McLennan, S.M., 1985. The Continental Crust: Its Composition and Evolution: An Examination of the Geochemical Record Preserved in Sedimentary Rocks. Blackwell Scientific.
Teal, L., Benavides, A., 2010. History and geologic overview of the Yanacocha Mining District, Cajamarca, Peru. Econ. Geol. 105, 1173–1190.
Tessalina, S.G., Plotinskaya, O.Y., 2017. Silurian to Carboniferous Re-Os molybdenite ages of the Kalinovskoe, Mikheevskoe and Talitsa Cu- and Mo porphyry deposits in the Urals: implications for geodynamic setting. Ore Geol. Rev. 85, 174–180.
Tu, X.L., Zhang, H., Deng, W.F., Ling, M.X., Liang, H.Y., Liu, Y., Sun, W.D., 2011. Application of resolution in-situ laser ablation ICP-MS in trace element analyses. Geochimica v. 40, 83–98.
Ulrich, T., Gunther, D., Heinrich, C.A., 1999. Gold concentrations of magmatic brines and the metal budget of porphyry copper deposits. Nature 399, 676–679.
Wang, Y., Fan, W., Zhang, G., Zhang, Y., 2013. Phanerozoic tectonics of the South China Block: Key observations and controversies. Gondwana Res. 23, 1273–1305.
Wang, S.H., Pei, R.F., Zeng, X.H., Qiu, X.P., Wei, M., 2009. Metallogenic series and model of the Zijinshan Mining Fiel. Acta Geol. Sin. 83, 146–157.
Waters, P.J., Cooke, D.R., Gonzales, R.I., Phillips, D., 2011. Porphyry and Epithermal Deposits and Ar^{40}/Ar^{39} Geochronology of the Baguio District, Philippines. Econ. Geol. 106, 1335–1363.
White, W.H., Bookstrom, A.A., Kamilli, R.J., Gangster, M.W., Smith, R.P., Ranta, D.E., Steininger, R.C., 1981. Character and origin of climax-type molybdenum deposits. Econ. Geol. 270–316.
Wu, Q., Cao, J., Kong, H., Shao, Y., Li, H., Xi, X., Deng, X., 2016. Petrogenesis and tectonic setting of the early Mesozoic Xitian granitic pluton in the middle Qin-Hang Belt, South China: Constraints from zircon U-Pb ages and bulk-rock trace element and Sr-Nd-Pb isotopic compositions. J. Asian Earth Sci. 128, 130–148.
Wu, L.Y., Hu, R.Z., Qi, Y.Q., Zhu, J.J., 2013. Zircon LA-ICP-MS U-Pb ages and geochemical characteristics of quartz syenite porphyry from Jintonghu deposit in Zijinshan ore field, Fujian Province, South China. Acta Petrol. Sin. 29, 4151–4166.
Wu, F.Y., Yang, Y.H., Xie, L.W., Yang, J.H., Xu, P., 2006. Hf isotopic compositions of the standard zircons and baddeleyites used in U-Pb geochronology. Chem. Geol. 234, 105–126.
Xiao, A.F., Li, D.M., Liu, X.M., 2012. LA-ICP-MS Zircon U-Pb Dating for the Volcanic Rocks of the Lower Formation of the Shimaoshan Group and Evolution of the Cretaceous Magmatism in the Zijinshan Cu-Au Orefield, Fujian Province. Geotectonica et Metallogenia 36, 613–623.
Xie, C.T., Zhou, M.J., 1994. Geological Characteristics of Luoboling Porphyry Copper (Mdydbenum) Deposit in Shanghang County, Fujian Province. Geol. Fujian 13, 151–158.
Xu, C., Chen, H., Huang, W., Qi, J., Duan, G., Zhang, L., Wu, C., Zhang, S., Zhong, W., 2017. Mesozoic multiphase magmatism at the Xinan Cu–Mo ore deposit (Zijinshan Orefield): Geodynamic setting and metallogenic implications. Ore Geol. Rev. 88, 768–790.
Xue, K., Ni, S.K., 2008. Geological Characteristics and Genesis of the Luobuling Copper (Molybdenum) Deposit in Zijinshan Orefield, Fujian. Resour. Environ. Eng. 22, 491–496.
Yu, B., Pei, R.F., Qiu, X.P., Chen, J.H., Li, D.P., Zhang, W.H., Liu, W.Y., 2013. The Evolution Series of Mesozoic Magmatic Rocks in the Zijinshan Orefield, Fujian Province. Acta Geol. Sin. 34, 437–446.
Zhang, J.J., 2013. Geology, exploration model and practice of Zijinshan ore concentrated area. Mineral Deposits v. 32, 757–766.
Zhang, D.Q., Li, D.X., Feng, C.Y., 2002. Porphyry-epithermal deposit system in Zijinshan orefield. Mineral Deposits 536–539.
Zhang, D.Q., Li, D.X., Zhao, Y.M., Chen, J.H., Li, Z.L., Zhang, X.K., 1991. The Zijinshan deposit: the frist example of quartz-alunite type epithrmal deposit in the continent of China. Geol. Rev. 37, 481–491.
Zhang, D.Q., Li, D.X., Feng, C.Y., Dong, Y.J., 2001. The Temporal and spatial framework of the mesozoic magmatic system in Zijinshan Area and its geological significance. Acta Geol. Sin. 22, 403–408.
Zhang, D.Q., She, H.Q., Li, D.X., Feng, C.Y., 2003. The Porphyry-epithermal metallogenic system in the Zijinshan Region, Fujian Province. Acta Geol. Sin. 77, 253–261.
Zhang, D.Q., Feng, C.Y., Li, D.X., She, H.Q., Dong, Y.J., 2005. The evolution of ore-forming fluids in the porphyry-epithermal metallogenic system of Zijinshan area. Acta Geosci. Sin. 26, 127–136.
Zhao, X.L., Mao, J.R., Chen, R., Xu, N.Z., Zeng, Q.T., Ye, H.M., 2007. Zircon SHRIMP age and geochemical characteristics of the Caixi pluton in southwestern, Fujian Provinc. Acta Petrologica et Mineralogica 26, 223–231.
Zhao, X.L., Mao, J.R., Chen, R., Xu, N.Z., 2008. SHRIMP zircon dating of the Zijinshan pluton in southwestern Fujian and its implications. Geol. China v. 35, 590–597.
Zhong, J., Chen, Y.J., Pirajno, F., Chen, J., Li, J., Qi, J.P., Li, N., 2014. Geology, geochronology, fluid inclusion and H-O isotope geochemistry of the Luoboling Porphyry Cu-Mo deposit, Zijinshan Orefield, Fujian Province, China. Ore Geol. Rev. 57, 61–77.
Zhong, J., Chen, Y.J., Chen, J., Qi, J.P., Dai, M.C., 2018. Geology and fluid inclusion geochemistry of the Zijinshan high-sulfidation epithermal Cu-Au deposit, Fujian Province, SE China: implication for deep exploration targeting. J. Geochem. Explor. 184, 49–65.
Zhou, S., Chen, H.S., 1996. Geochronology and geological significance of the Zijinshan copper-gold deposit. Bull. Mineral.: Petrol. Geochem. 15, 216–219.
Zou, Y., Chen, X., Huang, W., Zhang, J., Liang, H., Xu, J., Chen, L., 2017. Identification of an Early-Middle Jurassic oxidized magmatic belt, south Gangdese, Tibet, and geological implications. Sci. Bull. 62 (12), 888–898.